

ADDITIVE MANUFACTURING OF YSZ AND LITHIUM SILICATE
ELECTROCERAMICS FOR ENERGY GENERATION AND STORAGE

BY

JOHN TOWNSHEND HYDE CLARKE ZAENGLER

A THESIS
SUBMITTED TO THE FACULTY OF

ALFRED UNIVERSITY

IN PARTIAL FULFILLMENT OF THE REQUIREMENTS
FOR THE DEGREE OF

MASTER OF SCIENCE

IN

MATERIALS SCIENCE AND ENGINEERING

ALFRED, NEW YORK

APRIL 2021

ADDITIVE MANUFACTURING OF YSZ AND LITHIUM SILICATE
ELECTROCERAMICS FOR ENERGY GENERATION AND STORAGE

BY

JOHN TOWNSHEND HYDE CLARKE ZAENGLE

B.S. ALFRED UNIVERSITY 2019

SIGNATURE OF AUTHOR_____

APPROVED BY_____

S. K. SUNDARAM, ADVISOR

TIMOTHY KEENAN, ADVISORY COMMITTEE

JUNJUN DING, ADVISORY COMMITTEE

WILLIAM CARTY, CHAIR, ORAL THESIS DEFENSE

ACCEPTED BY_____

GABRIELLE G. GAUSTAD, DEAN
KAZUO INAMORI SCHOOL OF ENGINEERING

Alfred University theses are copyright protected and may be used for education or personal research only. Reproduction or distribution in part or whole is prohibited without written permission from the author.

Signature page may be viewed at Scholes Library,
New York State College of Ceramics, Alfred University,
Alfred, New York.

ACKNOWLEDGMENTS

I want to thank my advisor, Dr. S. K. Sundaram, for his guidance and support throughout my masters. Dr. Sundaram's drive for innovation has been instrumental in sparking my interest in electroceramics as well as fueling my interest in the sciences. I want to thank my committee members, Dr. Tim Keenan, and Dr. Junjun Ding, for their backing, support, and knowledge. I also would like to thank Dr. Scott Misture for inspiring deep thoughts and emphasizing connections within science and Dr. William Carty for inspiring pride and confidence in my work and, more so, my abilities. Alfred University has provided me with six wonderful years with many learning experiences. The community that Alfred University fosters helped drive me to pursue my interest in materials science and engineering. Lithoz America has provided an excellent insight into LCM printing with detailed explanations to questions regarding the CeraFab 3D printing system and the LCM process in general. I want to thank my friends and colleagues for being there for me both in the lab and outside. And lastly, I would like to express my gratitude to my family for their never-ending support, encouragement and for giving me the background, I needed to succeed.

TABLE OF CONTENTS

	Page
ACKNOWLEDGMENTS.....	III
TABLE OF CONTENTS.....	IV
LIST OF TABLES.....	VI
LIST OF FIGURES.....	VII
ABSTRACT.....	X
I. INTRODUCTION	1
1. <i>Ink-Jet Printing of Thin Film Ceramics</i>	1
2. <i>Lithography-based Ceramic Manufacturing (LCM)</i>	2
3. <i>Solid Oxide Fuel Cell</i>	4
4. <i>Yttria Stabilized Zirconia</i>	6
5. <i>Lithium Silicate</i>	7
6. <i>Lithium Silicate Synthesis</i>	9
II. EXPERIMENTAL PROCEDURE	12
1. <i>Powder Preparation</i>	12
2. <i>X-Ray Diffraction (XRD)</i>	13
3. <i>BET Measurements</i>	13
4. <i>Slurry Development</i>	14
5. <i>3D Printing</i>	14
6. <i>Post Printing Processing</i>	16
7. <i>Scanning Electron Microscopy (SEM)</i>	18
8. <i>Density and Porosity Testing</i>	18
9. <i>Electrical Conductivity</i>	19
III. RESULTS AND DISCUSSION	20
1. <i>YSZ Powders and Slurry Development</i>	20
a. Inframmat Advanced Materials YSZ Powders	21
b. Tosoh YSZ Powders	24
c. Slurry Development	25
2. <i>Printing and Sintering</i>	26
3. <i>Lithium Silicate</i>	44
4. <i>Electrical Conductivity</i>	56
IV. SUMMARY AND CONCLUSIONS	64
V. FUTURE WORK	65
VI. REFERENCES	66

LIST OF TABLES

	Page
TABLE I - Tosoh YSZ parts sintering profile 1.....	17, 27
TABLE II - Tosoh YSZ parts sintering profile 2.....	17, 29
TABLE III - Lithium silicate sintering profiles (* not included in profile).....	17, 51
TABLE IV - Tosoh powder-based test slurries.....	25
TABLE V - Tosoh YSZ sintered grain size.....	35
TABLE VI - Lithium silicate slurries.....	48
TABLE VII - Lithium Silicate Density and Grain Size.....	53
TABLE VIII – Bulk activation energy experimental vs literature values	61

LIST OF FIGURES

	Page
Figure 1. Basic schematic of a solid oxide fuel cell ⁴	4
Figure 2. Phase diagram for YSZ ⁶	6
Figure 3. Si-Li-O Phase Diagram ¹⁶	9
Figure 4. Parts in Lithoz CeraFab slicer program.....	15
Figure 5. Schematic example of printed layer orientation	19
Figure 6. Inframat nanopowder at 30.8 vol % solid loading (left) and Inframat	
superfine powder at 30.8 vol % solid loading (right)	22
Figure 7. Inframat RTP powder at 33.3 vol % solid loading.....	22
Figure 8. Inframat superfine ZrO ₂ (left, 10 µm scale bar) and nano ZrO ₂ (right,	
10 µm scale bar)	23
Figure 9. Inframat RTP ZrO ₂ without a binder (left, 20 µm scale bar) and RTP	
ZrO ₂ with a binder (right, 250 µm scale bar)	23
Figure 10. XRD results of three different Inframat powders, PDF 01-083-9463 ²⁰	24
Figure 11. YSZ slurry solid loading summary	26
Figure 12. Tosoh TZ-8YS 42.5 vol % sintered parts.....	27
Figure 13. Tosoh TZ-8YS MS13B 45.5 vol % sintered parts.....	28
Figure 14. Tosoh TZ-8YS 46.5 vol %, printed parts (left) and sintered parts (right).....	29
Figure 15. Tosoh TZ-8YS MS13B 48.5 vol %, printed parts (left) and sintered part	
(right).....	30
Figure 16. Tosoh TZ-8YS MS8 45.5 vol % sintered parts.....	31
Figure 17. Tosoh TZ-8Y MS8 40 vol % sintered parts.....	32
Figure 18. Tosoh TZ-8Y MS13B 40 vol % sintered parts.....	32
Figure 19. Tosoh TZ-8Y sintered parts compared to the starting powder,	
PDF 01-083-9463 ²⁰	33
Figure 20. Tosoh TZ-8YS powder comparison to the layer and smooth surface of	
sintered parts, PDF 01-083-9463 ²⁰	34

Figure 21. Tosoh TZ-8YS powder (left) and TZ-8Y powder (right).....	35
Figure 22. Tosoh TZ-8YS 42.5 vol% preconditioned parts, surface (left) and layer (right) all TZ-8YS slurries were made with MS13B Lithoz binder unless noted	36
Figure 23. Tosoh TZ-8YS 42.5 vol% sintered parts, surface (left, 10 µm scale bar) and layer (right, 50 µm scale bar)	37
Figure 24. Tosoh TZ-8YS 45.5 vol% preconditioned parts, surface (left, 5 µm scale bar) and layer (right, 500 µm scale bar)	37
Figure 25. Tosoh TZ-8YS 45.5 vol% sintered parts, surface (left, 10 µm scale bar) and layer (right, 20 µm scale bar)	38
Figure 26. Tosoh TZ-8YS MS8 45.5 vol% preconditioned parts, surface (left, 20 µm scale bar) and layer (right, 50 µm scale bar)	38
Figure 27. Tosoh TZ-8YS MS8 45.5 vol% sintered parts, surface (left, 10 µm scale bar) and layer (right, 50 µm scale bar)	39
Figure 28. Tosoh TZ-8YS 46.5 vol% preconditioned parts, surface (left, 20 µm scale bar) and layer (right, 50 µm scale bar)	39
Figure 29. Tosoh TZ-8YS 46.5 vol% sintered parts, surface (left, 10 µm scale bar) and layer (right, 10 µm scale bar)	40
Figure 30. Tosoh TZ-8YS 48.5 vol% preconditioned part surface (left, 20 µm scale bar) and sintered part surface (right, 5 µm scale bar)	40
Figure 31. Tosoh TZ-8Y MS13B 40 vol % preconditioned parts, surface (left, 20 µm scale bar) and layer (right, 100 µm scale bar)	41
Figure 32. Tosoh TZ-8Y MS13B 40 vol % sintered parts, surface (left, 5 µm scale bar) and layer (right, 50 µm scale bar)	41
Figure 33. Tosoh TZ-8Y MS8 40 vol% preconditioned parts, surface (left, 10 µm scale bar) and layer (right, 50 µm scale bar)	42
Figure 34. Tosoh TZ-8Y MS8 40 vol% sintered parts, surface (left, 5 µm scale bar) and layer (right, 10 µm scale bar)	42

Figure 35. Lithium silicate batch five after calcining.....	43
Figure 36. Lithium silicate powder, batch five (MD-208, left, 20 µm scale bar)	
and batch one (MD-203, right, 20 µm scale bar)	44
Figure 37. Lithium silicate Batch one to five powder XRD comparison, Li ₄ SiO ₄ -PDF	
00-020-0637 ²⁰ , Li ₂ SiO ₃ -PDF 00-029-0828 ²⁰ , and Li ₂ CO ₃ -PDF 04-010-7186 ²⁰ ...	
.....	45
Figure 38. Printed lithium silicate part comparison from start to finish of batch 5,	
Li ₂ SiO ₃ -PDF 00-029-0828 ²⁰ , Li ₂ CO ₃ -PDF 04-010-7186 ²⁰ , and SiO ₂ -PDF	
00-046-1045 ²⁰ unmarked peaks are Li ₄ SiO ₄ -PDF 00-020-0637 ²⁰	46
Figure 39. Lithium silicate sintering varied sintering temperature results. Peaks	
marked using Li ₂ SiO ₃ -PDF 00-029-0828 ²⁰ , Li ₂ CO ₃ -PDF 04-010-7186 ²⁰ ,	
and SiO ₂ -PDF 00-046-1045 ²⁰ unmarked peaks are	
Li ₄ SiO ₄ -PDF 00-020-0637 ²⁰	47
Figure 40. Lithium silicate MD-203 slurry in printer deemed too thick.....	48
Figure 41. MD-208 lithium silicate, parts (left) and slurry impression in the vat	
After (right)	49
Figure 42. MD-208 lithium silicate parts cleaned before preconditioning	
(both 10 mm scale bars)	50
Figure 43. MD-208 lithium silicate part preconditioned, surface	
(left, 50 µm scale bar) and layer (right, 10 µm scale bar)	51
Figure 44. Sintered lithium silicate from sintering profile four front (left) and back	
(right)	52
Figure 45. Sintered lithium silicate from sintering profile five front (left) and back	
(right)	52
Figure 46. Lithium silicate sintered part profile one, surface	
(left, 20 µm Scale Bar), and layer (right, 20 µm scale bar)	54
Figure 47. Lithium Silicate sintered part profile two, surface	
(left, 40 µm scale bar) and layer (right, 40 µm scale bar)	54

Figure 48. Lithium silicate sintered part profile three, surface	55
(left, 50 μm scale bar) and layer (right, 50 μm scale bar)	
Figure 49. Lithium silicate sintered part profile four, surface	56
(left, 100 μm scale bar) and layer (right, 150 μm scale bar)	
Figure 50. Lithium silicate sintered part profile five, surface	56
(left, 50 μm scale bar) and layer (right, 100 μm scale bar)	
Figure 51. Gold-coated lithium silicate (left), Tosoh TZ-8Y (middle), and Tosoh	57
TZ-8YS (right) samples after impedance testing	
Figure 52. Lithium silicate test sample in furnace with impedance test leads.....	58
 Figure 53. Lithium silicate surface at 200°C bulk and grain boundary resistance	
curve fit	59
Figure 54. YSZ surface at 400 °C bulk and grain boundary resistance curve fit	60
Figure 55. Arrhenius plot for Tosoh YSZ samples bulk and grain boundary	62
activation energy	
Figure 56. Arrhenius plot for lithium silicate samples bulk and grain boundary	62
activation energy	

ABSTRACT

Additive manufacturing (AM) of electroceramics is of interest because electroceramics are an excellent fit for solid oxide electrolytes. Faster material testing through the use of rapid prototyping made available through advances in additive manufacturing is now available. This investigation summarizes work on two materials of interest for energy generation and storage applications, fully stabilized 8 mol % yttria-stabilized zirconia (YSZ) and lithium silicate powders printed with a Lithoz CeraFab 8500 lithography-based ceramic slurry printer. This thesis focuses on variations in base powder, binder system, solids loading, heating profile, layer thickness, and layer orientation. Final part density, porosity, grain size, resistance, conductivity, activation energy, and crystal structure were measured to determine both the viability of 3D-printing and the effects the layers might have on microstructure.

Tosoh TZ-8YS powders mixed with Lithoz MS13B binder at a solid loading of 46.5 vol % sintered at 1450 °C resulted in highly dense uniform parts with no noticeable variations in bulk resistance, conductivity, or activation energy due to layering. Lithium silicate powders mixed with Lithoz MS13B binder at a solid loading of 51 vol % sintered at 800 °C resulted in dense parts with surface abnormalities and no noticeable variations in bulk resistance, conductivity, or activation because of layering.

The results show that base powder, binder system, solids loading, and layer thickness are important for 3D-printing. Slurry viscosity with a solid loading between 40 and 50 % is controlled by powder, solids loading, and binder. Microstructure and successful densification of samples depend on powder quality, heating profile, layer orientation, and binder system. In addition, the layering does not have a direct impact on the electrical properties of 3D-printed parts.

I. INTRODUCTION

Additive manufacturing (AM) has significantly advanced since the late 1990s, with different techniques showing promise for use with advanced materials previously deemed too expensive and difficult to machine. The term AM is referring to how a part is made in 3-dimensional (3D) space. When a material is added to the piece's body rather than subtracted from the piece to get the desired shape, that fabrication process is considered as AM. The development of lithography-based manufacturing opened new possibilities for powdered material fabrication as well as inkjet printing.

Stereolithography incorporates the use of photosensitive resins to form 3D-printed parts. The printer adds layers of material in the desired shape for that layer to the part. With powders' addition to the resin forming a "slurry," parts are made by hardening the binder therefore creating desired shape. Inkjet printing uses powder suspensions as printable inks. Both lithography and inkjet printing use a powder within a printable suspension material. Lithography, however, uses much higher solid loading at roughly 40 to 50 vol %, where inkjet uses 1 to 10 vol %. Once the part is 3D-printed, careful heating of the part allows the resin or ink to be burned out, and the remaining structure begins to sinter together. As the part is heated further, the powder densifies, forming a final monolithic solid part. This process has been successfully applied to ceramics, which are known for their strength and high-temperature stability. In addition, the ceramic parts are quite difficult to machine once densified and green processing beforehand can be challenging for complex shapes.

1. Ink-Jet Printing of Thin-Film Ceramics

Inkjet printers have been successfully used to print yttria-stabilized zirconia (YSZ) ceramics¹. Inkjet printers can also be used to create thin-film lithium-ion parts^{2,3}. Huang *et al.*² fabricated lithium-doped nickel oxide meshes using inkjet printing and Kang *et al.*³ fabricated a pouch type thin film lithium-ion battery using screen printing. Screen printing also uses ceramic suspensions "inks" to create a thin film. The printer relies on nano-sized ceramic powders in a fluid suspension. Typically, water, alcohol, or acid is used to create a ceramic ink. Other materials can also be added to act as dispersants. The ink produces a thin film on the print surface. The fluid used to hold the

ceramic powders in suspension is then burned out. Fine powders can prove challenging to disperse. Similar problems that occur in lithography slurries. However, lithography slurries do not need as fine of powders because they are not extruded through a fine nozzle as small as 20 μm wide as in inkjet printing¹. An inkjet printer relies on a nozzle to deposit the ink onto a surface forming a layer, multiple passes are used to build up layer thickness and increases powder density. However, the overall thickness of the part is about 1 - 2 μm in comparison to a lithography printer, where layers range over 15 - 150 μm and can build up thousands of layers. The thinner layers can allow for varying material layers to be printed. Materials such as YSZ can be directly deposited to an anode or cathode to form an electrolyte. However, thin layers can lead to flaws, e.g., holes, in the final dense parts¹. The lower solid loading of inks or slurries leads to a need to overlap layers to fill any voids in the powder structure. The voids, if left, affects the grain growth during sintering. The final dense part would have a low density and affect the electrolyte performance¹. Lithography, however, has higher solid loading helping to achieve highly dense parts.

2. Lithography-based Ceramic Manufacturing (LCM)

The LCM process originated from research from the Vienna University of Technology, and from there the company Lithoz GmbH was started in 2011. The Lithoz CeraFab 8500 is an LCM printer, a ceramic version of a stereolithography (SLA) printer. An LCM printer uses a projection system to cure a photosensitive resin one layer at a time to create a 3D model. A slicer software creates an image for each layer of the part; this allows for one whole layer to be printed and cured at a time. There is no difference in print speed if a part has a large or small area because the layer is done in one section rather than having something raster back and forth to create a layer as done in fused deposition modeling (FDM) a common plastic printing. However, the printing time depends primarily on the number of layers being printed, as more layers mean more cycles need to be completed by the printer. Layer thickness also directly affects the printing time for a print as thinner layers mean more layers need to be printed to achieve the same overall thickness. The part is printed upside down as the resin is a liquid and is stored in a vat below the build platform but above a projection system. The vat has a clear

bottom so the light from the projection system can pass into the slurry to cure it. A platform is used to raise and lower the build plate into and out of the slurry vat. The part is attached to the build plate. Once a part is lifted out of the vat, gaps in the slurry need to be filled.

A blade is employed to level and fill in the slurry gaps and form a uniform layer depth. The Z-axis limitations are based on how accurate the platform used to hold the part is. The X-Y plane accuracy depends on the resolution of the projection system fitted to the printer. The CeraFab has a lateral resolution of 40 μm and lateral dimensions of 80mm in the Y-direction and 120mm in the X-direction. The vertical layer resolution is between 15 and 150 μm with a vertical build height of 170mm. The layer height varies depending on slurry properties and the vertical resolution needed for the part being printed. LCM is a proven AM technique for ceramics, with the ability to vary print parameters and to print with various ceramic powders.

AM has become synonymous with rapid prototyping of 3D models. With advanced material printers like the CeraFab, AM can now be applied to rapid prototyping and manufacturing of energy materials and devices, e.g., fuel cells and batteries. The ability to manufacture precise test pieces quickly with minimal waste can help accelerate the development of advanced material-reliant products like solid oxide fuel cells (SOFC) and batteries. LCM and inkjet printing are proven AM methods; with variations in the ceramic parts being produced. Inkjet parts are very thin, leading to low density; however, different materials can be layered, leading to electrolytes being printed directly on electrodes. LCM parts are thicker and are produced from materials with much high solid loading, which allows for highly dense parts. Highly dense parts are needed for electrolytes because the defects such as pores and cracks will adversely affect electrical properties and device performance. LCM is used to study AM because highly dense ceramic parts can be produced using this process. However, the printing process creates a layered structure, which is retained in parts after sintering. Impedance testing is a valuable tool to determine the effects the layers have on the electrical conductivity of the samples produced.

3. Solid Oxide Fuel Cell

An SOFC is simply a device that converts chemical energy into electrical energy⁴.

A SOFC is comprised of a porous cathode where oxidation takes place and a porous anode where reduction occurs⁵. In between the anode and cathode is a solid electrolyte, which transports oxygen ions from the cathode to the anode. The electrolyte needs to remain both chemically and structurally stable at high temperatures as well as survive the chemical and structural stresses on each side caused by the electrodes. Figure 1 is an illustration showing how fuel and oxygen are fed into a fuel cell.

The incoming flow of oxygen into the cathode supplies oxygen ions to the electrolyte from a reduction reaction that occurs in the cathode. The oxygen ions flow through the electrolyte to the anode. A chemical oxidation reaction occurs with the supplied fuel such as hydrogen, which forms electricity and H₂O as a byproduct. Hydrocarbons are also an attractive fuel source for SOFCs because the energy density liquid fuels have is much higher than that of a gas source. Liquid fuels are common and have an expansive distribution network already in place for traditional combustion engines.

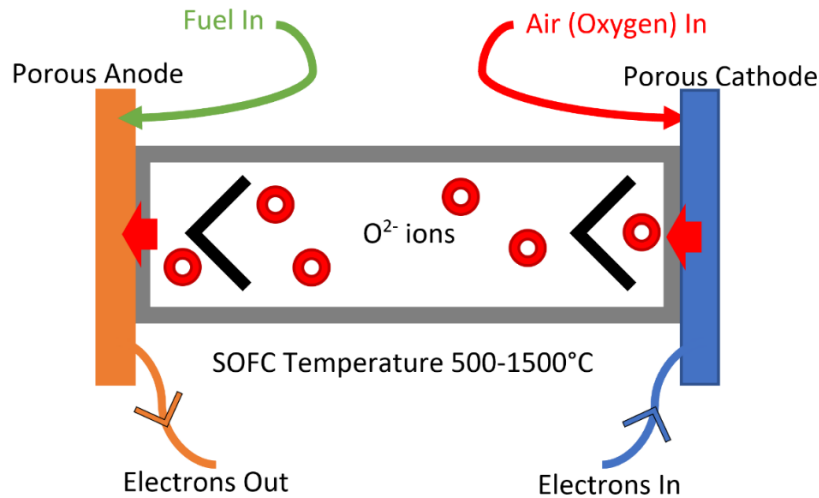


Figure 1: Basic schematic of a solid oxide fuel cell⁴.

SOFCS require clean fuels compared to combustion devices because the reaction depends on an efficient chemical reaction in the anode, so SOFCs are more efficient with less pollution than their combustion counterparts. Diesel, a common fuel for engines, can

be used in SOFCs but needs to be very high purity. More impurities in the fuel lead to anodes in the cell becoming contaminated and unusable. In diesel, a common impurity is sulfur, which needs to be removed from the fuel, making its use in SOFCs more costly. High-purity fuels can improve anode life expectancy and performance, but they are challenging to get and expensive to process. The use of different anodes that are less likely to react with common impurities may also be an alternative to current nickel anodes commonly used. Lastly, using a fuel that naturally has a high purity and readily available such as natural gas, could be a path towards standardized SOFCs. Natural gas can also be compressed, forming liquefied natural gas (LNG), which has improved energy density than standard gases.

Walther Nernst became famous for developing the Nernst lamp, a doped zirconia rod proving oxides exhibiting strong ionic conduction in the 1890s⁴. However, using ZrO₂ in a fuel cell did not come around until the late 1930s by Baur and Preis⁴. With current anode development not started until the 1960s⁴ and current cathodes not until the 2000s⁴. However, with the rise of AM, more anode, cathode, and electrolyte combinations can be tested. Electrolytes need to meet not just the ionic conductivity criteria required for an SOFC but also have high electric resistance so that ions flow through the electrolyte rather than back into it. Modern fabrication techniques such as 3D-printing will aid in another property for electrolytes which are low ionic resistance typically achieved by having the electrolyte in very thin layers. Low ionic resistance is needed to allow for oxygen atoms to move from the cathode to the anode unrestricted. Durability and cost are the last major factors that should be met when developing an electrolyte.

In an SOFC, the electrolyte acts as a check valve allowing for an efficient flow of oxygen atoms from the cathode to the anode. While allowing ion movement, the electrolyte also needs to create a seal between the cathode and anode so that gases and fuel do not permeate through interfering with the anode and cathode. The electrolyte density is important because a highly dense material both seals better and improves oxygen ion diffusion¹. Electrolytes need many octahedral interstitials to allow for proper ion flow through the structure⁴. Electrolytes also need to be electrically resistive to limit

the flow of electrons back through the electrolyte from the anode to the cathode. YSZ demonstrates both ionic conductivity and electrical resistivity.

4. Yttria Stabilized Zirconia (YSZ)

YSZ has proven a viable electrolyte material in the past because of its abundance, stability, and cost. YSZ has a cubic fluorite structure; the addition of yttria stabilizes the zirconia in the cubic phase. Figure 2 shows how the yttria addition in the material contribute to formation of more cubic phase. The 8 mol % YSZ is fully stabilized because the addition of yttria at elevated temperatures holds the zirconia structure in a cubic phase; commonly available 3 mol % YSZ is only partially stabilized.

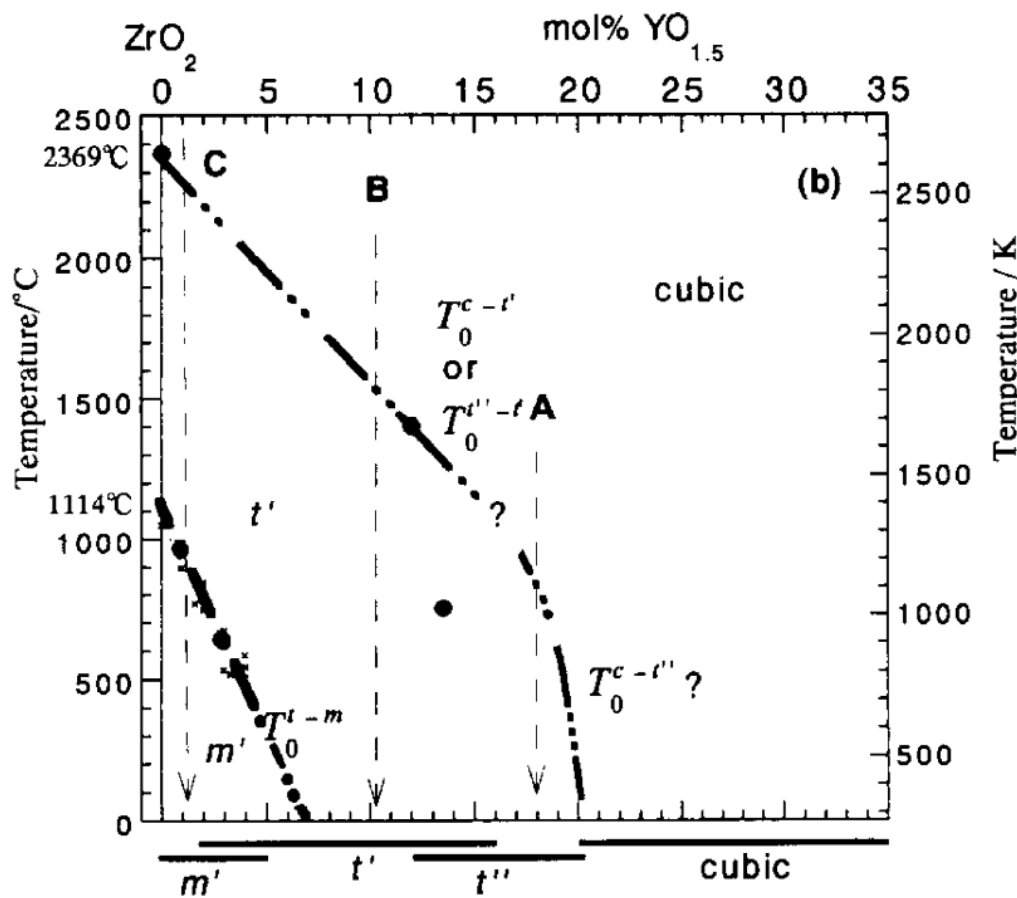


Figure 2: Phase diagram for YSZ⁶.

Pure ZrO_2 has very few intrinsic defects and has a monoclinic structure at room temperature. The ZrO_2 structure transforms first to triclinic above 1170°C and then to

cubic above 2370°C⁴; these phase transitions lead to property and volumetric changes in the material. When the material is fully stabilized in the cubic phase, changes are no longer a problem. The cubic phase is important for ion conductivity because dopants like yttria increase intrinsic defects in the structure⁴. The defects create vacancies for the oxygen ions to hop on as they move through the structure. This ionic conductivity typically increases at elevated temperatures, with the mechanical properties of YSZ remaining the same⁷. The resistance to heating is an important property for SOFCs because electrolyte temperature regulation becomes less important. With more stable electrolytes, optimal reduction and oxidation reaction temperatures can be used. However, reducing the operating temperature for SOFCs has been a primary focus of recent research to improve the usability and broaden potential applications⁸. Never less, electrolytes like 8 mol % YSZ with good thermal and chemical stability are important, leading to the continued interest in YSZ for SOFC⁸.

YSZ has been used to improve the internal combustion engine, a competitor/predecessor to the SOFC. The material is used to make oxygen sensors to determine oxygen concentration in exhaust gases. Both the ionic conductivity and thermal stability of YSZ make it ideal for O₂ sensor applications. The O₂ sensor helps improve the combustion efficiency of fuel in the engine by giving data to optimize the amount of air and fuel in the engine during operation.

The 3 mol % YSZ powder currently available commercially is only partially stabilized. Inkjet based printing is the only type of AM of 8 mol % or fully stabilized zirconia parts¹ reported to literature¹, the present study is an early attempt to AM 8 mol % YSZ using the LCM printing method.

5. Lithium Silicate

Lithium silicate, or more specifically lithium orthosilicate (Li₄SiO₄), is a lithium-ion conducting electroceramics. Lithium silicate can be used as an electrolyte for lithium batteries, CO₂ absorption/capture, as well as solid tritium breeding applications⁹⁻¹¹. The ceramic material is favorable for tritium breeding and CO₂ capture because the microstructure easily accommodates these processes¹¹. Solid tritium is becoming important because it is a fuel for first-generation fusion reactors; as fusion technology

develops, the need for fuel will increase, leading to an increased need for lithium silicate⁹. Before fusion technology becomes feasible, the combustion of fossil fuels remains. Reducing CO₂ emissions has become a high priority this century, with methods of removing CO₂ from significant sources like industrial facilities becoming a necessity. Lithium silicate traps CO₂ via formation of lithium carbonate. Thus, the CO₂ can be captured as concentrated CO₂ gas when the lithium carbonate is heated. The remaining material structure returns to the original lithium silicate, which can then be reused to capture more CO₂ repeating the process. The CO₂ can then be stored keeping it out of the atmosphere. The high lithium atom density as well as the Li⁺ interstitials and vacancies have made lithium silicate a material of interest for solid electrolytes in lithium-ion battery development^{9, 12}.

Lithium silicate can be used as a solid-state electrolyte in solid-state batteries. As energy storage has improved over the past two decades, high capacity and performance batteries are becoming more widespread. The development of physically stronger and more temperature-resistant batteries capable of high cycle rates have become important target for battery development. The high-lithium content of Li₄SiO₄ ceramics makes it an ideal electrolyte candidate¹³ for use at elevated temperatures integrating well with oxide electrode materials¹³. Lithium silicate has a monoclinic structure with lithium vacancies that allow for lithium-ion conduction, which creates the battery's output power; more the vacancies, better the conduction, and higher the more power the battery produces^{10, 13}. Cation dopants can be added to the structure; the dopants replace Li or Si atoms, allowing for more Li vacancies to form¹⁴. The addition of dopants improves the conductivity of lithium silicate.

Lithium containing ceramics have had some preliminary success with regards to AM with experimental testing using ink-based printing. Inkjet, direct ink writing, and screen printing have all been used to create anode, cathode, and electrolyte parts for battery applications^{2, 3, 15}. LCM printing has yet to be applied to lithium silicate powders. The present study is an early attempt at utilizing AM to fabricate lithium silicate using LCM for battery applications.

6. Lithium Silicate Synthesis

A solid-state reaction (SSR) is the most common method of synthesizing Lithium silicate^{10, 16}. Sol-gel is another method for synthesizing lithium silicate using chemical reactions rather than thermal reactions¹⁰. Figure 3 shows a ternary phase diagram from silicon, lithium, and oxygen showing the different compounds and phases the structure goes through during lithiation to form Li_4SiO_4 ¹⁷.

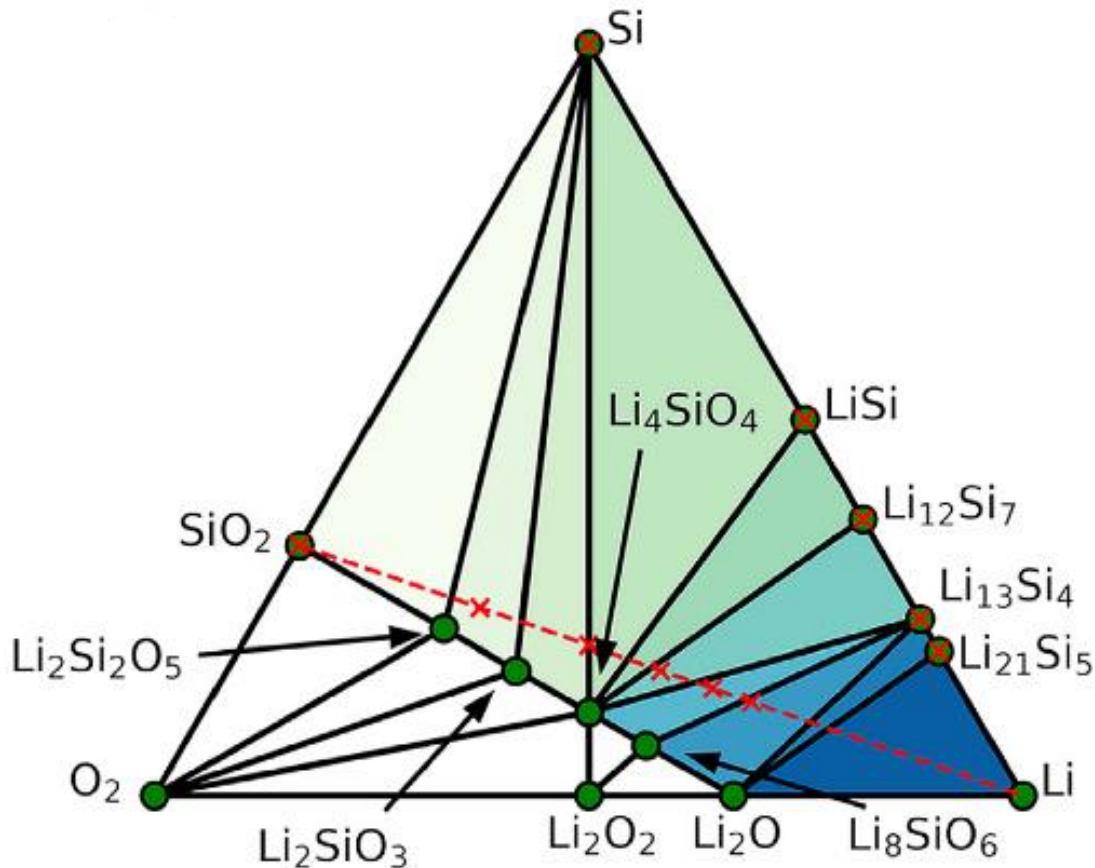
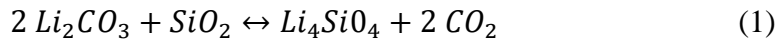


Figure 3: Si-Li-O Phase Diagram¹⁷.

SSR is a relatively simple method for synthesizing of lithium silicate because it works by heating a mixture of lithium carbonate and silicon oxide together in the right stoichiometry. At elevated temperatures, typically above 700°C, the mixture reacts to form, lithium orthosilicate and carbon dioxide. This process is applied to CO₂ capture, where lithium silicate is held at an elevated temperature between 400 and 500°C^{11, 16, 18}. At those temperatures, the lithium silicate absorbs CO₂ and reverts back to Li₂CO₃. Once

the temperature is brought back above 700°C the, lithium carbonate releases the CO₂ and forms Li₄SiO₄ again¹¹, as shown in the reaction (1).



However, the elevated temperature required to initiate the SSR can lead to problems such as agglomeration, volatilization, and contamination^{10, 12, 16}. When the material is being used for CO₂ absorption, the high temperatures are not an issue as the SSR reaction is used to release the CO₂ once absorbed. Powders made using the sol-gel method benefit from being synthesized at lower temperatures, which helps maintain a high-level of purity of the resulting powders. The high-purity and low synthesis temperatures help limit Li-evaporation during synthesis, making powders made by sol-gel better when lithium-ion concentration is important⁹. Sol-gel, however, uses different precursors than an SSR. Lithium oxide or lithium hydroxide instead of lithium carbonate is used to form Li₄SiO₄. Water and citric acid are used as chelating agents^{10, 12}. The colloid solution is vaporized at 70 to 80°C forming a gel, which is dried at 150°C resulting in lithium silicate^{10, 12}. The resulting powder can be ground and sieved in the same way material made from an SSR would be.

The high temperatures that SSR requires to form lithium silicate may lead to less-than-ideal powders compared to a sol-gel powder. However, because the powders will be further processed into slurry for printing as well as need to be preconditioned and sintered at high temperatures, ultra-high purity lithium silicate via sol-gel process is not followed. SSR provides a consistent method of producing lithium silicate; powder surface area and size are more important for producing a printable slurry than lithium content.

This thesis summarizes the work done on fully stabilized 8 mol % YSZ and lithium silicate powders. These powders were tested to determine if the materials could successfully be made into slurries for use in an LCM 3D printer. Solid loading, powder morphology, and binder system were physical characteristics that were varied during test printing, along with adjustments to the print settings used to create test parts. Once printed, the parts were debinded and then sintered to form dense ceramic parts. Materials characterization tools were used to determine the phases present, structure, bulk conductivity, density, surface morphology, and grain size of the successfully 3D-printed

and sintered dense parts. The layering of the parts from the printing process was also studied to determine whether the layer orientation relative to surface-mounted electrodes affected the bulk conductivity of the dense parts. Finally, dense YSZ and lithium silicate parts were produced to demonstrate how the 3D-printing process affected the parts' microstructure and bulk conductivity.

II. EXPERIMENTAL PROCEDURE

1. Powder Preparation

Two materials, 8 mol% YSZ and lithium silicate (Li_4SiO_4), were selected for the present study. These materials were used in powder form to develop slurries for use in a Lithoz CeraFab 8500 SLA type 3D printer (Lithoz America. LLC, Troy, NY, USA). The YSZ powders were procured from Tosoh USA (Grove City, OH, USA) and Inframmat Advanced Materials LLC (Manchester, CT, USA) to make 11 slurries using different binder systems and powders of different sizes and surface areas. The lithium silicate was prepared using SSR of silica and lithium carbonate to form the powder used for printing.

YSZ powders from both Inframmat advanced materials and Tosoh Corporation were tested to determine if viable slurries could be developed for 3D-printing. The ideal powders needed to be $0.5\text{-}1 \mu\text{m}$ in size with a low surface area of roughly $5\text{-}7 \text{ m}^2/\text{g}$. Tosoh fully stabilized TZ-8YS grade powder was determined to have the best properties for initial slurry development and was paired with Lithoz MS13B binder. The TZ-8YS powders had a Brunauer-Emmett-Teller (BET) surface area result of $5.57 \text{ m}^2/\text{g}$. Later, Tosoh fully stabilized TZ-8Y powders were tested and found to form usable slurries. The TZ-8Y powders had a BET surface area of $13.69 \text{ m}^2/\text{g}$.

The Inframmat powders tested were superfine grade 8 mol% YSZ powder, nano 8mol% YSZ powder, and ready to press grade 8 mol% YSZ powder. The Inframmat powders had higher surface areas compared to the Tosoh powders. The ready to press powder also needed to have a PVA binder burnt out to allow the Lithoz binders to work correctly. However, once the binder was burnt out at 425°C for 5 h, the ready-to-press powders BET surface area was $40.40 \text{ m}^2/\text{g}$. Of the remaining two powders, the superfine grade had the lowest BET surface area of $20.87 \text{ m}^2/\text{g}$, with the nanopowder having a BET surface area of $43.29 \text{ m}^2/\text{g}$. All three powders resulted in very low solids loading, around 30-40 vol % is the lowest solid loading that still allows for useable parts from the Lithoz printer.

Lithium silicate powder was prepared by a solid-state reaction procedure described in previous works¹⁶. A mixture of 5:2 by weight of Li_2CO_3 (99%, Alfa Aesar)

and SiO₂ (99.5% Alfa Aesar) were mixed in 99% isopropyl alcohol for 40 minutes. The mixture was allowed to sit on a hot plate at 60°C overnight to evaporate the alcohol before being loaded into 150ml high form alumina crucibles. The crucibles were then placed into a box furnace to begin the reaction. Heating started at room temperature and ramped at a rate of 5°C/min. The sample was held at 680°C for 15 - 20 h. Dwell was determined by the batch size. Longer dwell times were needed for larger batches. Once complete, the furnace was cooled to room temperature naturally. The powders shrank and stuck together, forming a porous block, which was then broken up and sieved to below 45 µm. The powders were either ground by hand with a mortar and pestle or in a gyro mill (Glen Creston, London, England); however, the gyro mill resulted in some iron filings in the processed powders. The small amount of iron was removed with a magnet. The phase purity was confirmed using x-ray diffraction. However, small amounts of Li₂SiO₃ were present in the samples.

2. X-Ray Diffraction (XRD)

XRD was used on the three powders that resulted in a successful slurry: the TZ-8YS, TZ-8Y, and lithium silicate powders. The resulting patterns were used to confirm the phases of the powders. The diffractograms are presented in the results and discussion section. The x-ray diffractometer used was a Brucker D2 Phaser (Bruker, Billerica, MA, USA) using Cu-Kα radiation of 1.54056Å with a LYNXeye detector. The samples were rotated at 30rpm over the range of 10-80° 2θ with a 0.02 step size and count time of 0.5 seconds. All pattern fitting was done in Bruker Topas (Bruker, Billerica, MA, USA) with ICDD PDF4+ databases for patterns. Origin Pro (OriginLab Corporation, Northampton, MA, USA) was used to format XRD-.xy data into formatted plots.

3. BET Measurements

BET measurements were conducted using a Gemini VII surface area analyzer (Micromeritics, Norcross, GA, USA). Samples were first degassed in nitrogen for 1-2 h at 140°C before being measured.

4. Slurry Development

Five YSZ powders were tested to determine if viable slurries could be made. Three powders from Inframmat advanced materials were tested in three different binders from Lithoz with all combinations not exceeding 35 vol % solids loading. Printable slurries have a solid loading of at least 40 vol %. The Inframmat powders were dispersed in 99% isopropanol to break up large agglomerates before the powders were mixed with a binder. Two Tosoh powders were mixed with two binders from Lithoz to determine the maximum solid loading while remaining flowable enough to spread in the printer both Tosoh powders and Lithoz binders were deemed printable. Once a maximum solids loading was determined, a larger batch of 100 g was made and 3D-printed. The slurries were subjected to different energy levels to determine how the slurry cured and to what depth. The energy and corresponding depth data were used to create the print parameters used during actual 3D-printing.

Lithium silicate powders were mixed with Lithoz MS13B binder to form two slurry batches. The shelf life was very short; therefore, the resulting slurries needed to be used within the same week of being mixed with the MS13B binder. The slurry was subjected to varying energy levels to determine curing depths for printing.

5. 3D Printing

Slurries were printed using a CeraFab 8500 (Lithoz America LLC, Troy, NY, USA). The CeraFab printer used is equipped with a projection system with a resolution of 40 μm . The printer build area is 80 mm by 120 mm in the X. Y. and 170 mm in the Z-axis. The layer heights slurries were printed ranged 25-100 μm . Slurries were stored in a refrigerator before printing. The slurries needed to warm up to room temperature before being loaded into the printing vat as they became thicker at low temperatures. Roughly 10 – 15 g of slurry would be loaded into the vat once warm enough and be spread to a thickness of approximately 175 μm for YSZ prints and 275 μm for lithium silicate prints.

Once the correct slurry depth was achieved in the vat, the parameters were adjusted according to the tested slurry. The parts were loaded into the Lithoz slicer program as STL files and could be viewed as a 3D representation of an example build

area seen in Figure 4. The parts can be moved around the build area to allow for some control over the resulting parts. Hanging disks are an example of test parts that were printed to test layer orientation. They were printed perpendicular to the build area's y-axis to minimize potential rotational forces caused by the vat being lowered away at the end of each print layer. The rotation could potentially break the part off the build plate. The thickness of the layers varied over 20-150 μm depending on the slurries curing depth. The rotation of the vat and curing energy was also changed depending on slurry properties.

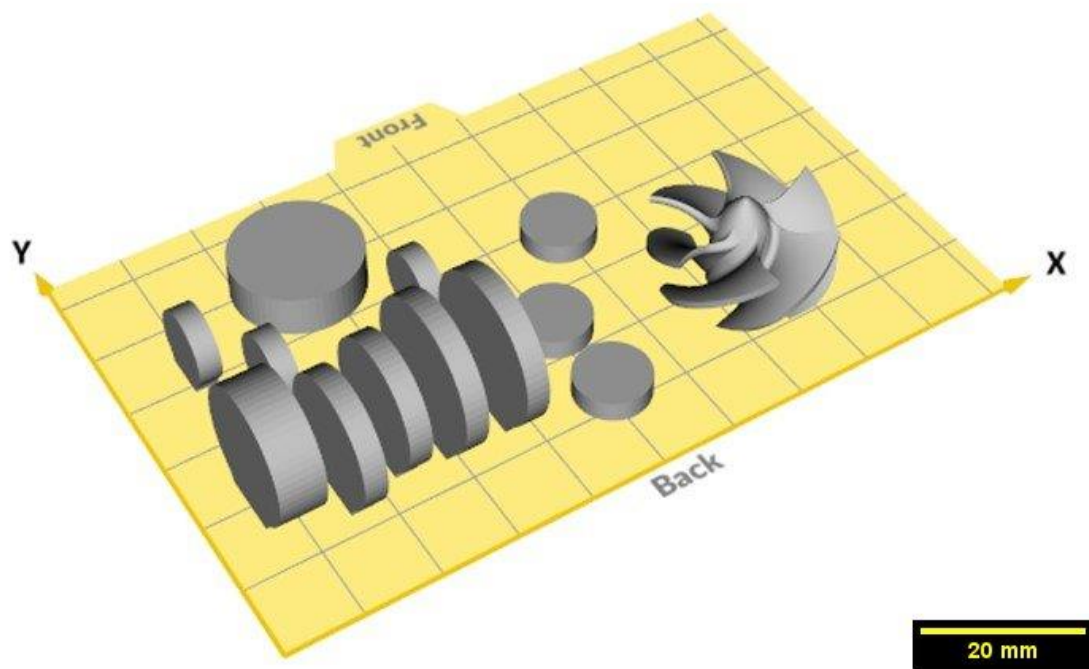


Figure 4: Parts in Lithoz CeraFab slicer program.

Thicker slurries spread better with slower rotation speeds and more rotations. Slurries with MS13B used higher curing energies because the MS13B binder included dyes that absorbed the blue light used to cure the slurry. Settling/resting time was also adjusted for thicker and thinner slurries, with longer settling times needed for the thicker slurries. The slurry vat itself also tilted down away from the part before the part was raised and lowered down; this helped avoid air bubbles from forming and keeps the parts firmly attached to the build plate. The speed the vat was raised or lowered and adjusted depending on the viscosity of the slurry in the vat. Once the settings were optimized for

the characteristics of the slurry, the print file was saved and opened on the CeraFab printer digital control panel and then the printing was started.

The build plate for the printer had a piece of LithaFoil (Lithoz America, LLC, Troy, NY, USA) applied to the surface along with a piece of electrical tape around the edge to prevent scattered light from escaping. LithaFoil was a thin mat plastic that was applied to the glass of the build plate. The plastic allowed for better adhesion of the part to the build plate while still allowing the part to be removed once the print was complete. Prints were typically conducted at 16 % humidity and a temperature range of 24-30 °C. Some thicker slurries needed to be warmed to the higher 30°C temperature in the printer to improve the viscosity so the slurry could be evenly spread in the vat. The heating was done using a small custom heater inside the printer that circulated warm air throughout the printer enclosure.

6. Post Printing Processing

The build plate was removed from the CeraFab printer and placed in a cleaning station. The parts were carefully removed from the LithaFoil layer on the build plate and then cleaned using LithaSol 20. Excess uncured slurry sticks to the part as it was printed and was cleaned off with LithaSol, which was sprayed onto the part with an airbrush. The airbrush was then used to blow the dissolved excess slurry off. The cleaned parts were dried and then placed in a HERAtherm oven (Thermo Fisher Scientific, Waltham, MA, USA) to precondition. Parts were preconditioned at 120°C for 2-4 days depending on the thickness of the part, thicker parts needed to be preconditioned longer. The YSZ parts were placed in a Carbolite RHF 1600 (Carbolite Furnaces, Sheffield, UK) box furnace and heated following two 8 step thermal profiles; TABLEs I and II were the two profiles used. At 420°C, the binder was burned out, and final sintering took place at 1450°C. The lithium silicate parts followed the same procedure to debind and sinter; however, the profile followed was different as shown in TABLE III. Once all parts were cooled, they were characterized.

TABLE I: Tosoh YSZ parts sintering profile 1.

Temperature (°C)	Ramp (°C/min)	Dwell (h)
140	0.1	4
170	0.2	4
250	0.2	2
420	0.3	0.01
500	1.2	0.01
600	1.7	0.01
1250	1.7	0.01
1450	3.3	2

TABLE II: Tosoh YSZ parts sintering profile 2.

Temperature (°C)	Ramp (°C/min)	Dwell (h)
135	0.1	16
170	0.2	4
225	0.2	6
325	0.3	4
420	1.2	4
600	1.5	1
1050	1.5	1
1450	2.5	2

TABLE III: Lithium silicate sintering profiles (* Not Included in Profile).

Temperature (°C)	Ramp (°C/min)	Dwell (h) Profile 1	Dwell (h) Profile 2	Dwell (h) Profile 3	Dwell (h) Profile 4	Dwell (h) Profile 5
130	0.1	3	3	3	3	3
170	0.1	3	3	3	3	3
220	0.1	4	4	4	4	4
250	0.2	5	5	5	5	5
325	0.2	5	5	5	5	5
430	0.5	2	5	5	5	5
680	1	*	*	*	*	5
700	1	*	*	*	5	*
800	1	*	*	5	*	5
900	1	4	5	*	5	*
120	Naturally Cooled	Naturally Cooled	Naturally Cooled	Naturally Cooled	Naturally Cooled	Naturally Cooled

7. Scanning Electron Microscopy (SEM)

Powder and part surface microstructures were analyzed using a Quanta 200 SEM (FEI Company. Hillsboro, OR, USA). Dry powders were attached to SEM sample holders using carbon tape for imaging. Printed parts were attached to SEM sample holders using carbon tape and then gold-coated using a Cressington 108 sputter coater (Cressington Scientific Instruments, Watford, UK) for 45-60 s at 10 mA and 0.06 mbar. Samples were then imaged in high vacuum, using a typical beam voltage of 15kV, the average spot size of 4 and an average working distance of 10.5 mm.

8. Density and Porosity Testing

American Standards and Testing Methods (ASTM) standard C20-00 for apparent porosity, water absorption, apparent specific gravity, and bulk density of burned refractory brick and shapes by boiling water¹⁹ was used for density and porosity measurements. Samples were placed in a drying oven overnight before initially weighing them. Next, samples were boiled in deionized water for three hours, with the water level periodically being topped off. After the three hours of boiling, the samples were kept submerged overnight before being weighed a second time. Samples were suspended in deionized water from the bottom of a scale for a suspended weight to be collected. The samples were weighed a third time to measure the saturated weight. The samples were removed from the water and patted dry, removing excess water from the surface before weighing. Once all three weights had been collected, calculations were carried out to determine apparent porosity and bulk density. Parts were assumed to be cylindrical and measured using a Mitutoyo ASX Caliper (Mitutoyo Corporation, Kawasaki, Japan). An average of two radius measurements were used when determining the radius for the volume calculation. Material density was measured using a AccuPyc II 1340 helium pycnometer (Micromeritics, Norcross, GA). The AccuPyc was used to find the real density of the materials making up the final parts. Sintered parts were ground into a fine powder and then tested. Density results were used to calculate the percent density for printed parts.

9. Electrical Conductivity

Impedance spectroscopy was used to determine the frequency-dependent conductivity of the 3D-printed sintered materials. A Solartron SI 1260 impedance analyzer (Ametek, Hampshire, UK) with a custom environmental chamber was used for these measurements. The applied voltage was 1V with a frequency range of 1 Hz to 10 MHz. Samples had gold electrodes applied on either side using a Cressington 108 sputter coater (Cressington Scientific Instruments, Watford, UK) for 1 minute at 10 mA and 0.06 mbar. YSZ samples impedance was measured over 100-800 °C at 50 °C increments.⁸ Lithium silicate samples impedance was measured over 25-300 °C at 25 °C increments.¹² Impedance spectra collected were analyzed using ZView software (Scribner Associates Inc, Southern Pines, NC, USA).

Figure 5 shows a schematic example of the two-layer orientations tested. The layers for the "surface" orientation were printed with the layers parallel to the disk face where the electrodes for impedance testing were placed. The layers for the "layer" orientation were printed with the layers perpendicular to the disk face where the electrodes were placed.

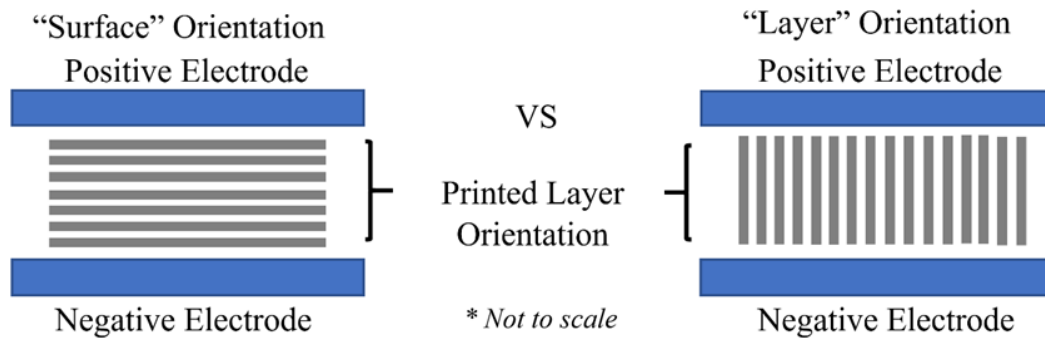


Figure 5: Schematic example of printed layer orientation.

III. RESULTS AND DISCUSSION

1. YSZ Powders and Slurry Development

Five YSZ powders were tested to determine if they could form a viable slurry. When developing a slurry, the ideal solid loading is generally in the range of 40 - 50 vol %. The reason for that window is when the slurry is printed, a binder is cured, which holds the powder in the 3D structure. The binder is burned out during after printing processing, leaving just the powders that will need to be sintered together to make a completed part. If too little powder is used in making the slurry, the powders will crumble during debinding and sintering. However, if too much powder is used, i.e., above 50 vol %, the slurry typically becomes too thick making it difficult to spread in the printer. Ideally, the powders have a low surface area and uniform particle size, both aids the viscosity of the slurry. The Lithoz system uses a blade to create a thin film of slurry with a specific depth, the overall viscosity of a slurry is an important factor. Particles with a size of roughly 0.5 - 1 μm are ideal. The size of the powder is important because it can hinder the viscosity of the slurry. Agglomeration can be a significant problem, but ideal powders disperse easily when mixed with binders during slurry production.

The two binders used in conjunction with the YSZ powders were Lithoz MS8 and MS13B. The MS13B was initially used with the Inframmat and Tosoh powders because it allowed for higher solid loading. The MS13B binder used had a red dye that absorbs the blue light used to cure the binder. The absorption of the light helps keep light scattering in the slurry down and can also help control the slurry's curing depth. However, the Inframmat powders never resulted in a printable slurry. The two Tosoh powders worked well with both the MS8 and the MS13B binders with each binder working better with one powder over another. The MS13B binder worked better with the larger particle size and smaller surface area of the Tosoh TZ-8YS powders. The MS8 binder worked better with the larger surface area and finer particle size of Tosoh TZ-8Y powder. The MS8 binder had no dye added to control light penetration and light scattering leading to deeper curing depths in the TZ-8Y powders. The TZ-8Y powders needed the improved penetration of the binder because of the higher surface area. The MS8 binder is also a straighter monomer chain, making the resulting parts more flexible, which helps in sintering for

parts with lower solid loading like the TZ-8Y slurries. The MS13B binder was highly crosslinked, making green parts much stiffer.

a. Inframmat Advanced Materials YSZ Powders

The first three powders tested were from Inframmat Advanced Materials (Manchester, CT, USA). The materials were a superfine grade 8 mol % YSZ powder, a nano 8mol % YSZ powder, and a ready to press grade 8 mol % YSZ powder. The three powders underwent BET measurements, XRD, and SEM imaging. The powders contained large hard agglomerates that could not be easily dispersed. The Tosoh powders, however, could be easily dispersed in the binder resin. BET measurements were used to determine the powder's surface area. The measured surface area was $40.40\text{ m}^2/\text{g}$ for the ready to press powders (RTP). The RTP powders also contained a PVA binder, which was burned out before any testing. The remaining two powders, the superfine grade, had a BET surface area of $20.87\text{ m}^2/\text{g}$, and the nanopowder $43.29\text{ m}^2/\text{g}$. When mixed with varying binders, all three powders resulted in very low solids loading of, 30 vol %. MS13B was the binder that showed the most promise with the Inframmat powders and was used as the primary binder used when testing the Tosoh powders. When the powders were mixed with MS13B, at best, they had a consistency similar to peanut butter. A good slurry has a consistency close to maple syrup. Figures 6 -7 are examples of how thick the slurries became after mixing. The yellow hue in the images is from the yellow lighting inside the lab, limiting slurry exposure to blue light. Blue light can cause the binders to cure partially.

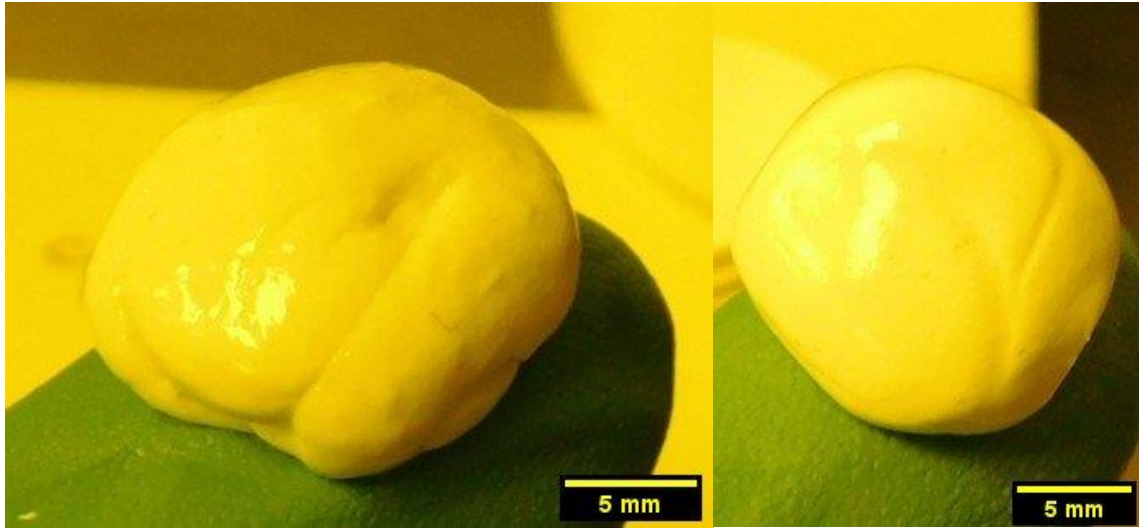


Figure 6: Inframat nanopowder at 30.8 vol % solid loading (left) and Inframat superfine powder at 30.8 vol % solid loading (right).

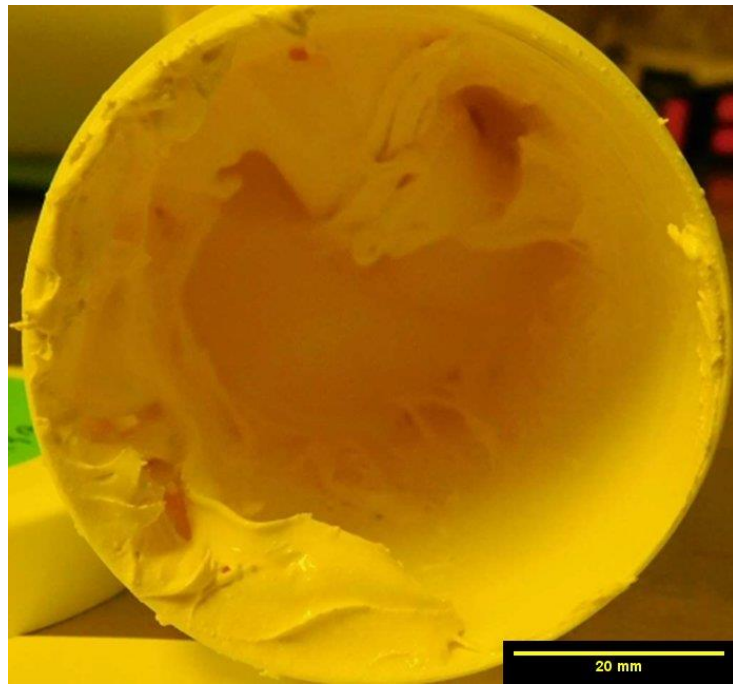


Figure 7: Inframat RTP powder at 33.3 vol % solid loading.

SEM images of the powders seen in Figure 8 showed relatively large individual particle sizes for the Inframat superfine powders. The superfine powder had less agglomeration than the nano and RTP powders. The Inframat nano-powders had large agglomerates that were found difficult to break down during mixing with different binders. Figure 9 shows the RTP powders with the binder burned out (left) and with the PVA binder still in the powder (right). With the binder burned out, a wide distribution of

particle size was observed in the RTP powders with smaller particles agglomerating together.

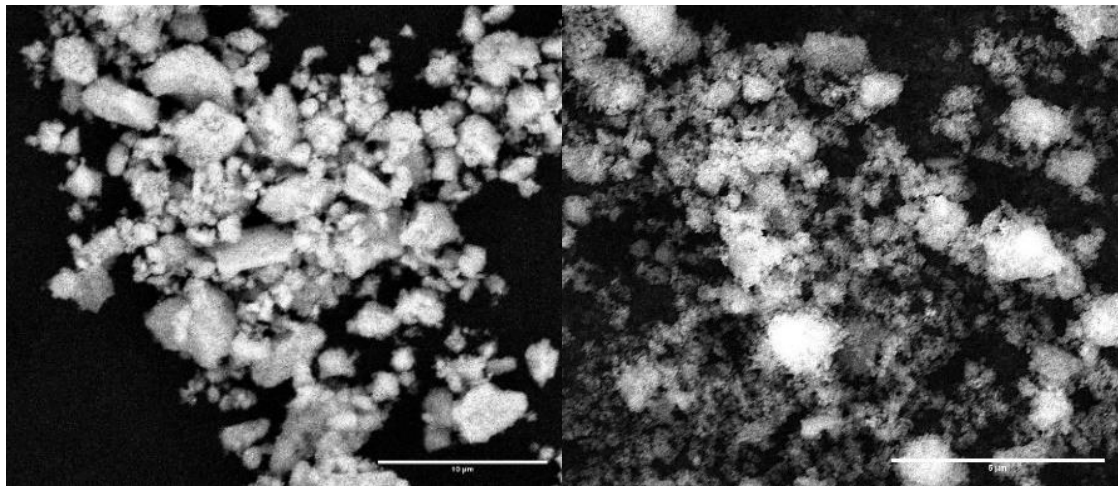


Figure 8: Inframmat superfine ZrO_2 (left, 10 μm scale bar) and nano ZrO_2 (right 10 μm scale bar).

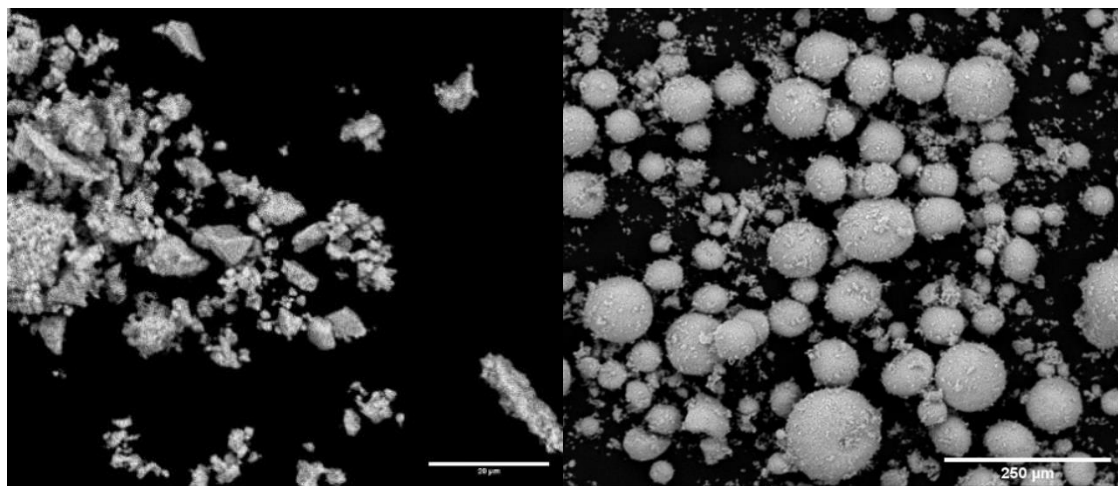


Figure 9: Inframmat RTP ZrO_2 without a binder (left, 20 μm scale bar) and RTP ZrO_2 with a binder (right, 250 μm scale bar).

The XRD data confirmed the powders were crystalline and had cubic zirconia peaks. The data, however, had additional peaks appearing as well as broader peaks, which, meant the powders were of lower quality compared to the Tosoh powders. All three Inframmat powders diffractograms are plotted in Figure 10, with slightly sharper peaks present in the nano and superfine powders.

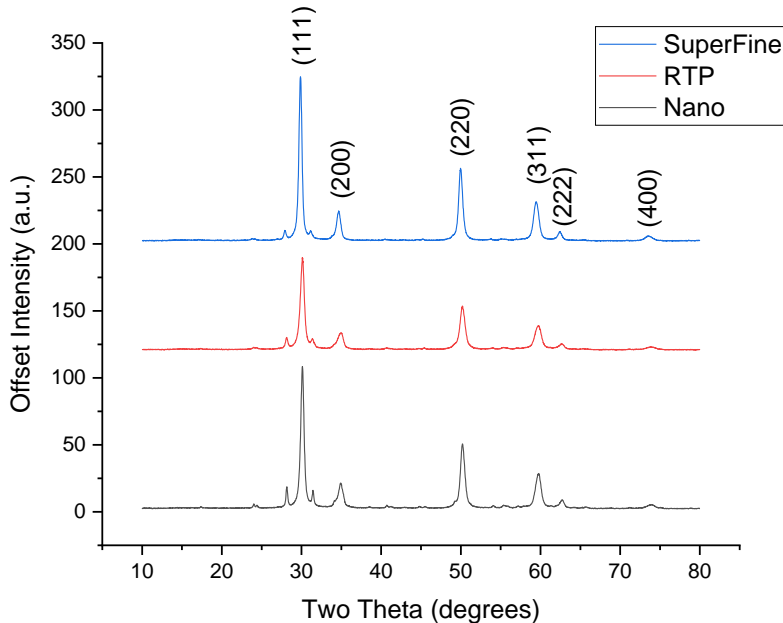


Figure 10: XRD results of three different Inframmat powders, PDF 01-083-9463²⁰.

b. Tosoh YSZ Powders

Two Tosoh zirconia powders were used to make printable slurries. Seven different slurry formulations consisting of either Tosoh TZ-8YS or Tosoh TZ-8Y powders were prepared for printing. The powders used were fully stabilized, primarily for solid oxide fuel cell applications. The seven variations tested focused on either the powder used, the binder used, or solid loading. The primary powder tested was the TZ-8YS powder because it was found to have a lower surface area compared to other 8 mol % zirconia powders tested. The lower surface area allowed for higher solid loading. The BET surface area measurements for TZ-8YS resulted in a surface of $5.57 \text{ m}^2/\text{g}$, which allowed for relatively high solids loading to be achieved, needed later during the thermal processing of samples. The maximum solid loading that TZ-8YS powders were printed with was 48.5 vol %, with 42.5 vol % being the lowest tested. The TZ-8Y powders resulted in a BET surface area of $13.69 \text{ m}^2/\text{g}$ and a tested solid loading of 40 vol %. The different binders that were tested were designated Lithoz MS13B and MS8. TABLE IV lists YSZ slurries used to print, with all slurries working to some extent.

TABLE IV: Tosoh powder-based test slurries.

Lithoz Batch Number	Powder	Binder	Solid loading (Vol %)	Bulk Density (%)
MD-193	Tosoh TZ-8YS	MS13B	42.5 vol%	97.9
MD-196	Tosoh TZ-8YS	MS8	45.5 vol%	95.3
MD-171	Tosoh TZ-8YS	MS13B	45.5 vol%	96.0
MD-143 +202	Tosoh TZ-8YS	MS13B	46.5 vol%	98.3
MD-195	Tosoh TZ-8YS	MS13B	48.5 vol%	97.2
MD-192 +194	Tosoh TZ-8Y	MS13B	40 vol%	92.5
MD-204	Tosoh TZ-8Y	MS8	40 vol%	93.4

c. Slurry Development

YSZ and lithium silicate test slurries were developed at Lithoz America LLC (Troy, NY, USA). Figure 11 is a summary of the consistency vs. solid loading of potential slurries with 4 different YSZ test powders and 3 proprietary binders. Figure 11 shows the variation in slurry based on binder and powder with regards to achieving a flowable slurry within the ideal solid loading requirements. Grindometer measurements were used to determine the consistency of the slurry and whether it would flow well in the printer. TZ-8Y powders were also tested with lower solid loading than the TZ-8YS powders but was still achieved a flowable slurry within the ideal solids range. The TZ-8Y had a higher surface area leading to the lower solid loading. The lithium silicate powders had issues with particle size and agglomeration causing slurry viscosity to change. Lithium silicate slurries had to be prepared and printed within the same week. Curing depth was determined for each slurry at varying exposure intensity (mJ/cm^2). This dataset was used to create a printing profile based on printing depth and other factors. YSZ powders needed no additional milling before binder addition. Lithium silicate was milled in the binder however the powder reacted with the resin causing the slurry to become too thick and viscous was unusable. The lithium silicate slurry that resulted in a printable slurry did not receive any additional milling from Lithoz.

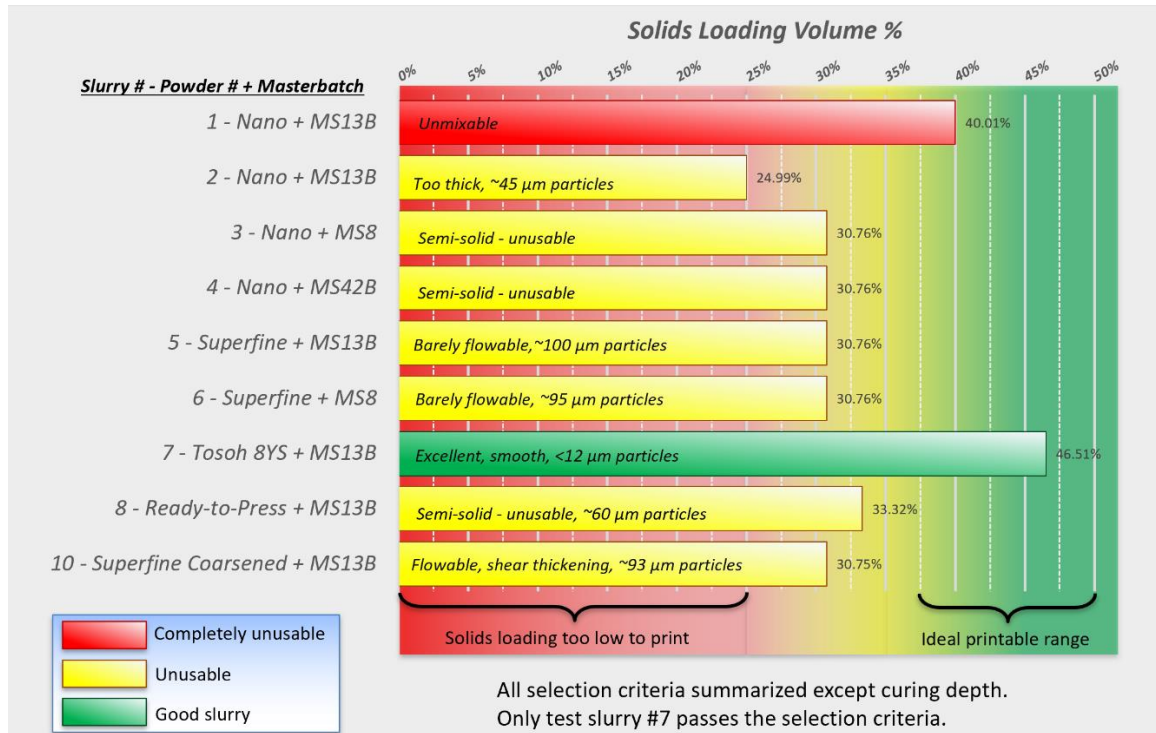


Figure 11: YSZ slurry solid loading summary.

2. Printing and Sintering

The MS13B binder printed well when combined with the TZ-8YS powders. TZ-8YS combined with MS13B was printed with a solid loading of 42.5 %, 45.5 %, 46.5 %, and 48.5 %. The 42.5 vol % slurry printed well and remained very fluid over the length of the print. The lower solid content allowed for easier printing because there was more binder, allowing for better curing and spreading. The 42.5 vol % parts were easily removed with no surface damage. Next, the parts were cleaned of residual slurry, dried, and moved into a drying furnace at 120 °C for three days. The drying furnace was used to precondition the parts and fully cure the binder system. The YSZ samples became more robust as they were conditioned because the binder was further cured. After the parts had been preconditioned, some small cracks appeared on the surface of larger, thicker parts as shown in Figure 12. The center part was a 17.5 mm × 6 mm hanging disk. The hanging disk parts were printed so each layer was printed perpendicular to the disk face. These parts can be identified by a foot on one edge of the disk, which is included to increase the initial area attached to the printer's build plate. Parts were sintered following the heating profile found in TABLE II.

Once fired, the parts with thin walls like the turbine found to the right in Figure 12 had no surface damage like cracks or flaking. The turbine was 18 mm in diameter and 10.5 mm tall. Parts with wide layers like the piece to the left in Figure 12, which was printed 17.5 mm wide and 3 mm tall, resulted in many layers flaking and cracking apart.

Bulk density was calculated using 10 mm diameter \times 3 mm high disk and 10 mm diameter \times 3 mm high hanging disk if samples were available. A disk that was printed flat to the build plate (standard disk) had a larger surface area per layer compared to a hanging disk that had many more layers in total but a smaller surface area per layer. Density calculations were used to determine if layer orientation had effects on how parts were sintered. For parts printed with TZ-8YS MS13B 42.5% solid loading slurry standard disk, the parts reached a density of 97.2% vs. hanging disk 98.6%, with an overall average of 97.9%. The theoretical sintered density of 5.9 g/cm³ for Tosoh TZ-8YS compared well with the actual calculated density of 5.94 g/cm³.

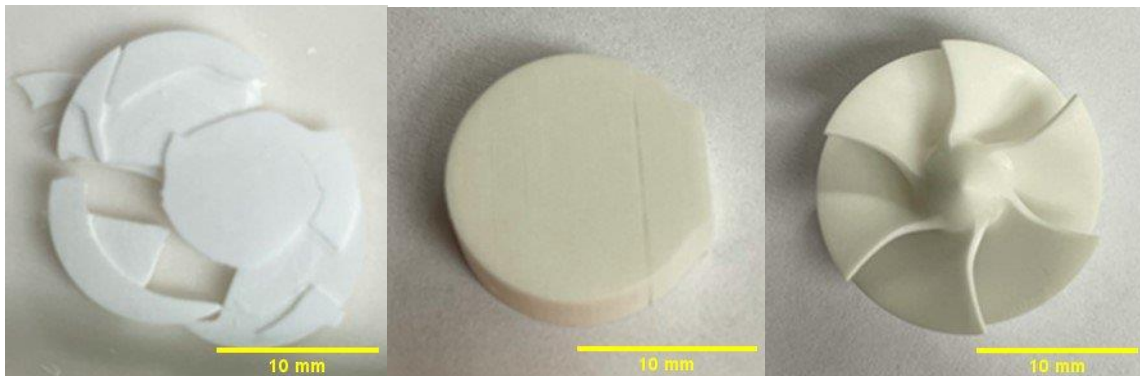


Figure 12: Tosoh TZ-8YS 42.5 vol % Sintered Parts.

TABLE I: Tosoh YSZ parts sintering profile 1.

Temperature (°C)	Ramp (°C/min)	Dwell (h)
140	0.1	4
170	0.2	4
250	0.2	2
420	0.3	0.01
500	1.2	0.01
600	1.7	0.01
1250	1.7	0.01
1450	3.3	2

Tosoh TZ-8YS MS13B 45.5 vol % slurry was considered one of the ideal mixtures. The solids loading was enough that sintering went well even with thicker parts but still low enough the slurry remained very flowable during printing. After printing, the parts were cleaned with LithaSol and preconditioned at 120°C for three days. The parts were sintered following the heating profile in TABLE I. The resulting parts shown in Figure 13 demonstrated successful sintering. The parts to the left are as printed a 10 mm × 6 mm disk and a 17.5 mm × 3 mm disk. In the middle are two 17.5 mm × 6 mm hanging disks. To the right is two 17.5 mm × 6 mm disks. The average density for the TZ-8YS MS13B 45.5% parts was 96.0%. The measured samples were both standard disks.



Figure 13: Tosoh TZ-8YS MS13B 45.5 vol % sintered parts.

Two Tosoh TZ-8YS MS13B 46.5 vol % slurries were prepared. The 46.5% slurries were considered the other ideal solid loading for the TZ-8YS powders. The prints printed well with fresh slurry. However, after being stored in a freezer for five months, the slurry became thicker and was challenging to work with. Successful prints were cleaned with LithaSol and preconditioned for three days at 120°C. The test parts were sintered following the heating profile in TABLE II. The resulting parts sintered well, even thicker parts such as a 10 mm × 10 mm cylinder. The standard disk density was 97.9%, where the hanging disk density was 98.8%, with the average being 98.3%. The left of Figure 14 is a batch of just printed parts with two turbines and two mesh parts used to determine how more complex geometries would print and densify. In the right of Figure 14 are fully sintered parts with the larger disk and hanging disk starting as 17.5

mm × 3 mm parts and the smaller disk and hanging disk being 10mm × 3mm. Both turbines and mesh pieces from the print sintered well.

TABLE II: Tosoh YSZ parts sintering profile 2.

Temperature (°C)	Ramp (°C/min)	Dwell (h)
135	0.1	16
170	0.2	4
225	0.2	6
325	0.3	4
420	1.2	4
600	1.5	1
1050	1.5	1
1450	2.5	2



Figure 14: Tosoh TZ-8YS 46.5 vol %, printed parts (left) and sintered parts (right).

Tosoh TZ-8YS MS13B 48.5 vol % slurry was used to determine a relative maximum printable solid loading using Tosoh TZ-8YS powders. The slurry resulted in completed parts however was very thick. The slurry viscosity was relatively high and got worse with printing. Because of the thickness, the blade in the CeraFab would abort from the high resistance caused by the thicker slurry. Because of this problem, only the 120-layer parts shown in Figure 15 were printed. The slurry needed to be spread at a slow speed because, at higher speed, it would pull towards itself, causing an uneven layer to form in the vat. To the left of Figure 15 are the parts after being printed, to the right is a 20 mm × 3 mm disk with layer flaking after sintering. The samples were cleaned with

LithaSol and preconditioned for three days at 120°C. They were then sintered following the heating profile in TABLE II. Two 10 mm × 3 mm disks were used for density calculations; the density was 97.2%.

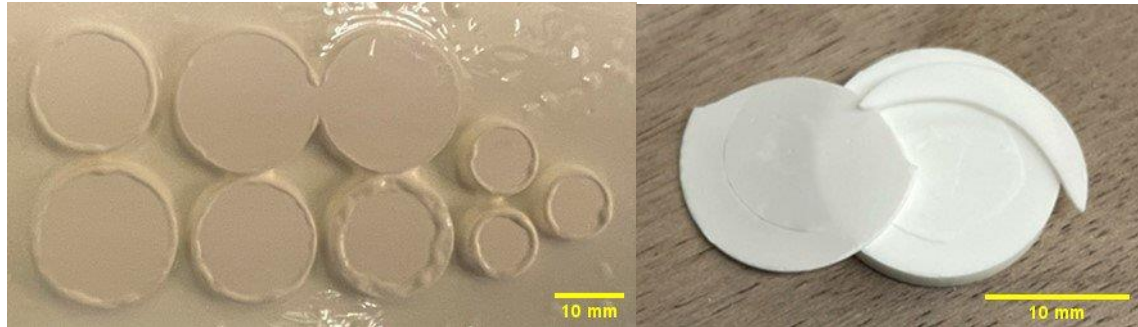


Figure 15: Tosoh TZ-8YS MS13B 48.5 vol %, printed parts (left) and sintered part (right).

MS8 binder was tested with TZ-8YS powders however did not print well as the slurries made with MS13B. Tosoh TZ-8YS powder was added for a solid loading of 45.5 vol %. The slurry was used for two prints; the first went relatively well, with the slurry becoming slightly thicker towards the end of the print, the total layer count was 120. The second print reused the residual slurry in the vat of the CeraFab. The second print made it to layer 63 before the slurry was utterly unusable, and the whole print was aborted. The standard disk had been fully printed with the abort only affecting the hanging disk. Similar to the 48.5 vol % slurry, the blade responsible for spreading the slurry would abort spreading because the slurry had become so thick. The completed and partially completed parts were cleaned with LithaSol and preconditioned for two days at 120°C. The parts were sintered following the heating cycle found in TABLE I. The parts in Figure 16 resulted in some cracking and warping in larger diameter parts. The leftmost image is an as-printed 17.5 mm × 3 mm disk that had cracked with the two middle views depicting the center and how it warped during sintering. The rightmost view is as printed 20 mm × 3 mm disk that had warped slightly during sintering but stayed intact.

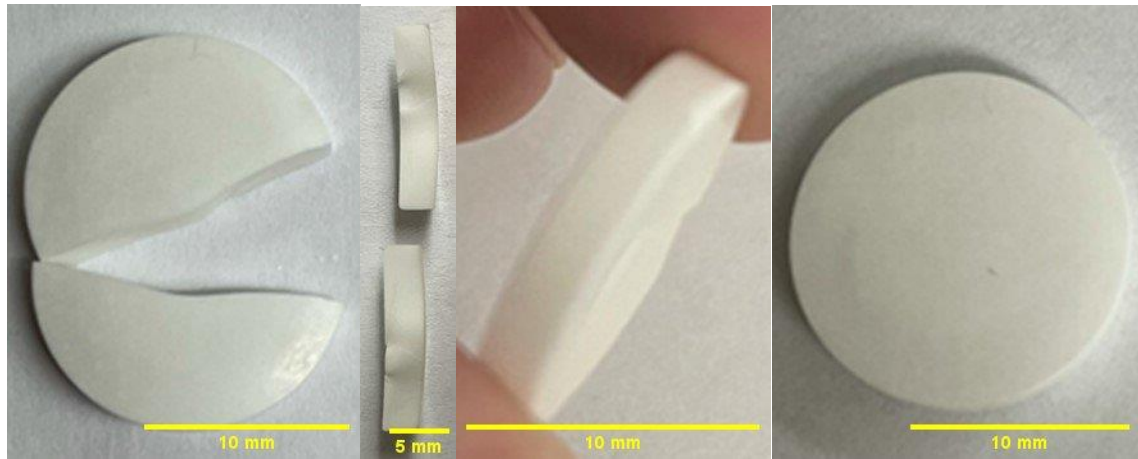


Figure 16: Tosoh TZ-8YS MS8 45.5 vol % sintered parts.

Tosoh TZ-8Y powders have a BET surface area over twice that of the TZ-8YS powders tested. The TZ-8Y powders are also smaller than the TZ-8YS powders²¹. When preparing slurries, a lower solid loading of 40 vol % had to be used. Tosoh TZ-8Y MS8 slurry resulted in the best parts. The slurry remained fluid during printing but needed to be warmed at first after being stored in a refrigerator for two weeks. Once the slurry had warmed up, it spread easily and was reused for a second print without any problems. A 10 mm tall hanging disk was printed successfully, which was the tallest / most layers printed with the slurry without any issues. Once printed, the parts were cleaned using LithaSol and preconditioned for three days at 120°C. The sintering profile is presented in TABLE II. In Figure 17, completed parts after the second print is to the left. The larger disk is 20 mm × 3 mm and 17.5 mm x 3 mm with some 10 mm × 3 mm disk. The bars printed were 3 mm × 3 mm and 30 mm long. A sintered 10 mm hanging disk can be seen to the right of Figure 16. The density for the hanging 10 mm × 3 mm disk was 92.9%, and the density for the standard 10 mm × 3mm disk was 93.9%. The average sintered density was 93.4%, which was the highest observed of all tested Tosoh powder-based slurries.

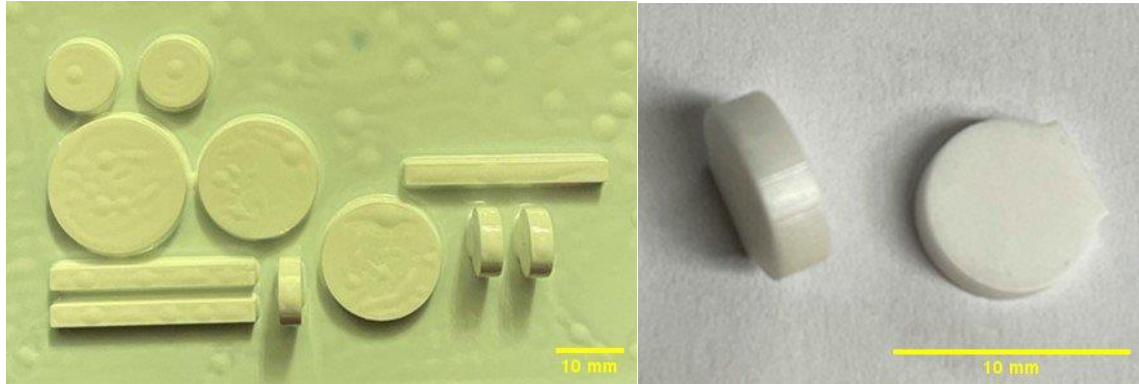


Figure 17: Tosoh TZ-8Y MS8 40 vol % sintered parts.

The Tosoh TZ-8Y powders were also tested with MS13B binders. The slurry tested was Tosoh TZ-8Y MS13B 40 vol %. The slurry printed well. However, it was thicker than MS8 based slurry. The parts were cleaned with LithaSol and preconditioned for three days at a temperature of 120°C. Once the parts had been preconditioned, some of the 20 mm × 3 mm and 17.5 mm × 3 mm hanging disk test pieces had formed visible surface cracks. The parts were sintered using the profile in TABLE I. Once the parts had cooled, a 6mm thick standard disk flaked entirely apart, which can be seen in the 17.5mm × 6mm disk to the left of Figure 18. Some of the smaller standard 10 mm × 3 mm disk stayed together or had some minor cracking. The larger hanging disk separated at the layers seen in the middle of Figure 18; the samples were 17.5 mm × 3 mm disk. However, some of the larger 20mm × 3mm hanging disks sintered successfully. The complex shape of the turbine successfully sintered. However, as seen in Figure 18, the blades are 0.75mm thick; the turbine's relatively thin walls helped improve the sintering survival. The density for a hanging 10 mm × 3 mm disk was 93.4%, and the density of a standard 10 mm × 3 mm disk was 91.6%. The average density was 92.5%.

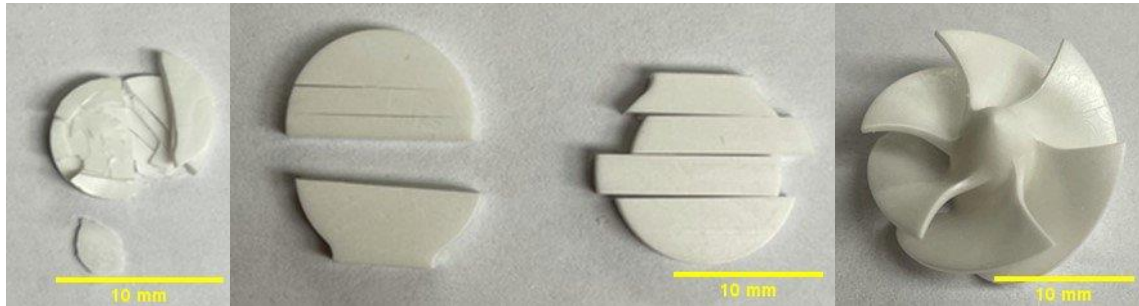


Figure 18: Tosoh TZ-8Y MS13B 40 vol % sintered parts.

Sintering schedule was adjusted slightly from TABLE I and TABLE II. With longer hold times at lower temperatures for TABLE II. A temperature of 420 °C was used for the binder burnout. TABLE III has lower ramp rates, so there is less stress in the part during sintering. The slower heating profile results were evident in the samples testing slurry mixtures with nonideal compositions. The 42.5% and 48.5% MS13B TZ-8YS slurries and the 45.5% MS8 TZ-8YS slurry were used to test either maximum or minimum solid loading and the results of a different binder. They showed better results if sintered following TABLE II. The slurries containing 45.5% or 46.5% MS13B TZ-8YS could be sintered with the faster TABLE I profiles but still resulted in better parts when sintered with the TABLE II profile. In addition, the TZ-8Y powders resulted in better parts when sintered at a slower rate.

XRD was used to confirm the cubic fluorite structure in the YSZ powders both before and after processing. The XRD plots are shown in Figures 19-20. PDF 01-083-9463²⁰ was used to confirm the 8 mol % YSZ cubic phase. An increase in crystallinity can be seen in the sintered parts with increased intensity in the peaks compared to the corresponding powder peaks.

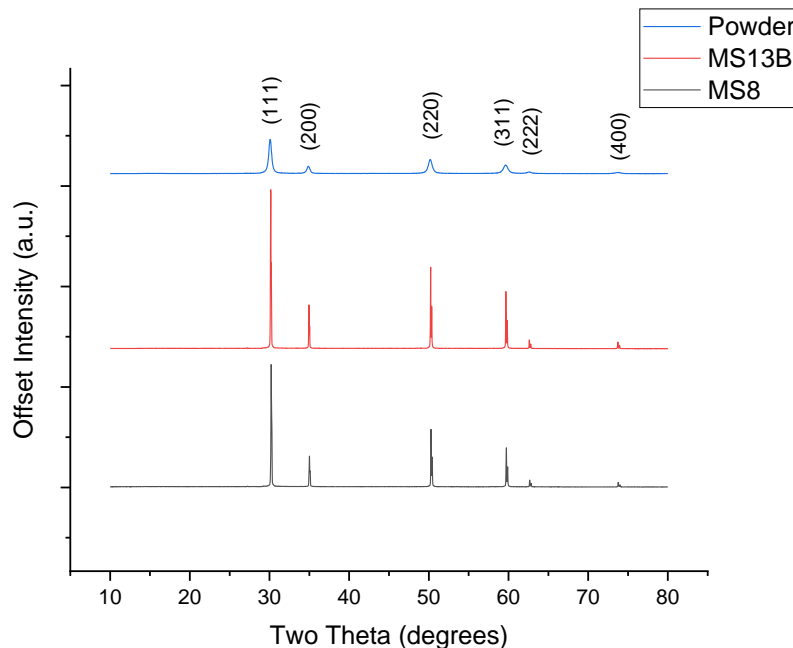


Figure 19: Tosoh TZ-8Y sintered parts compared to the starting powder, PDF 01-083-9463²⁰.

The XRD plots of the Tosoh TZ-8YS were nearly identical to the TZ-8Y plot, with a cubic fluorite structure identified. The diffractogram of the TZ-8YS prints shown in Figure 20 are for a comparison of the powder, a sintered part with a flat layer in the x-ray beam path, and a part's layered surface in the x-ray beam path. No changes in structure were identified after both printing and sintering of the parts. The sintered parts had sharper peaks than the powders, with no noticeable difference between the surface and the layered part.

The average particle size for Tosoh TZ-8YS was $0.5 \mu\text{m}^{21}$. The small size of the powders can be seen to the left of Figure 21. However, the Tosoh TZ-8Y powders are slightly smaller with an average size of $0.25 \mu\text{m}^{21}$ as seen to the right in Figure 21.

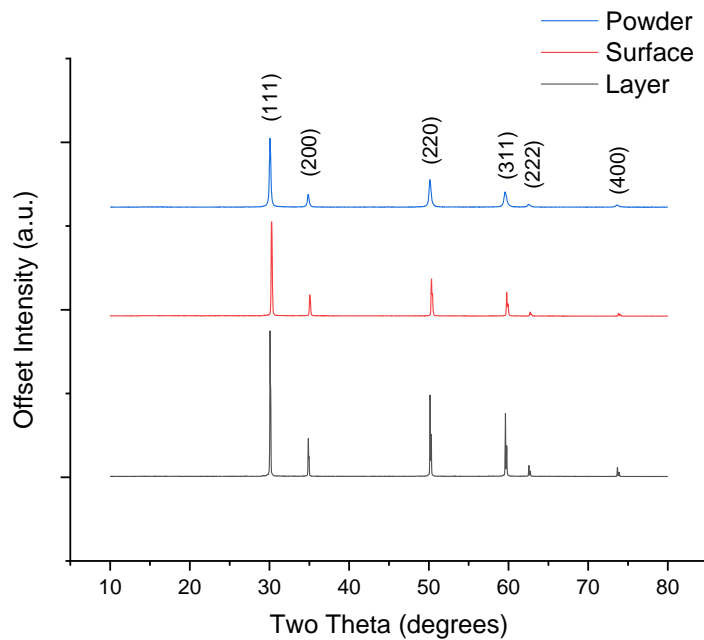


Figure 20: Tosoh TZ-8YS powder comparison to the layer and smooth surface of sintered parts, PDF 01-083-9463²⁰.

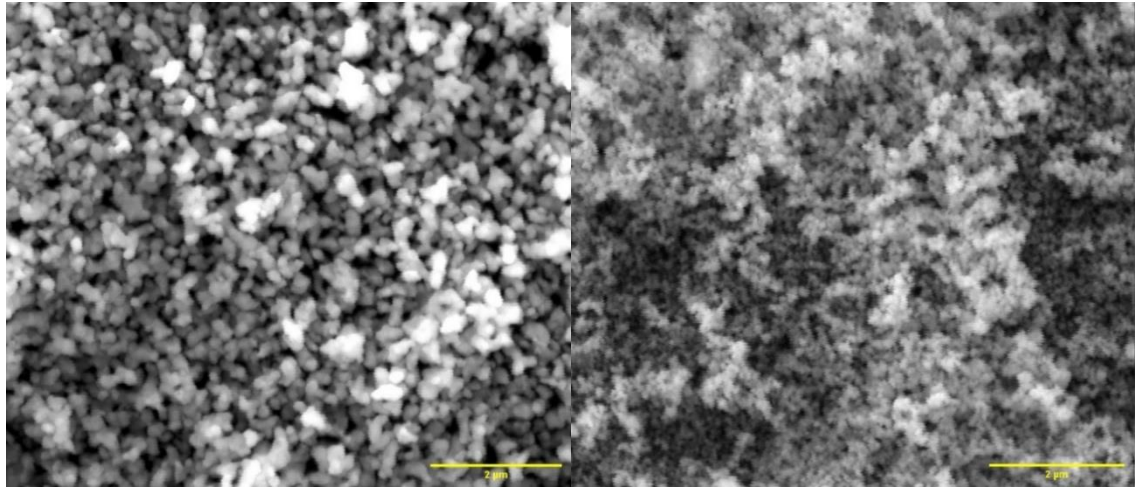


Figure 21: Tosoh TZ-8YS powder (left, 2 μm scale bar) and TZ-8Y powder (right, 2 μm scale bar).

The particle sizes and agglomeration affected the surface area and thus achievable solid loading of each powder. The TZ-8YS powders, as shown in Figure 21, have nice relatively spherical-shaped particles with no large agglomerates present. However, the TZ-8Y powders in Figure 21 have some agglomerates present with the smaller particles sticking together.

The two different particle sizes of the Tosoh powders produced samples with different grain sizes, as shown in TABLE V. The average grain size was measured using the linear intercept method⁸. The method involves a straight line being placed over a sample cross-section; the grains underneath the line are then measured, creating a randomized measurement. Samples were all measured with a correlation between particle size and grain size. The larger TZ-8YS powders resulted in smaller average grains at 2.7 μm . The TZ-8Y powders had better grain growth with an average of 5.3 μm .

TABLE V: Tosoh YSZ sintered grain size.

Slurry Solid Loading	42.5*	45.5*	45.5 MS8	46.5*	48.5*	40*	40 MS8
Average Grain Diameter	2.5 μm	3.7 μm	2.6 μm	2.5 μm	2.4 μm	6.0 μm	4.5 μm

* Made with Lithoz MS13B binder.

The Tosoh TZ-8YS samples had observed cracks between some of the printed layers, which did not densify together during sintering. Examples of this were seen in the

42.5 vol %, 45.5 vol %, and 46.5 vol % solid loading slurries. The 48.5% solid loading slurry only resulted in surface samples and no layered samples. The 48.5% slurry was viscous which resulted in poor prints. The slurries were initially printed with parts lying flat to the build plate with the largest surface area connected to the plate. Most test pieces were disks. The disk face was the surface connecting the piece to the build plate. Another reason for the larger area being printed parallel to the plate was more of the part was completed during each layer leading to fewer printed layers. The lower layer count improved print speed and allowed fewer chances for the print to fail from slurries becoming too viscous. Slurries containing 48.5 vol % solids were much more challenging to print because the viscosity was higher than slurries with lower solid loading. The viscosity led to problems of spreading the slurry, so no layered test samples were printed with 48.5 vol % slurry, so parts with low layer count had a high chance of being completed successfully.

Figures 22, 24, 26, 28, 30, 31, and 33 all show a surface view and close-up layer view of preconditioned YSZ samples. Figures 23, 25, 27, 29, 30, 32, and 34 show the sintered YSZ samples surface and layers. Figures 22-30 are the TZ-8YS samples with smaller grain sizes compared to the TZ-8Y samples in Figures 31-34. Cracks were easily identified in Figures 22, 23, 24, 25, and 26. Higher solid loading and the change from TZ-8YS to TZ-8Y powders resulted in a decrease in identifiable cracks.

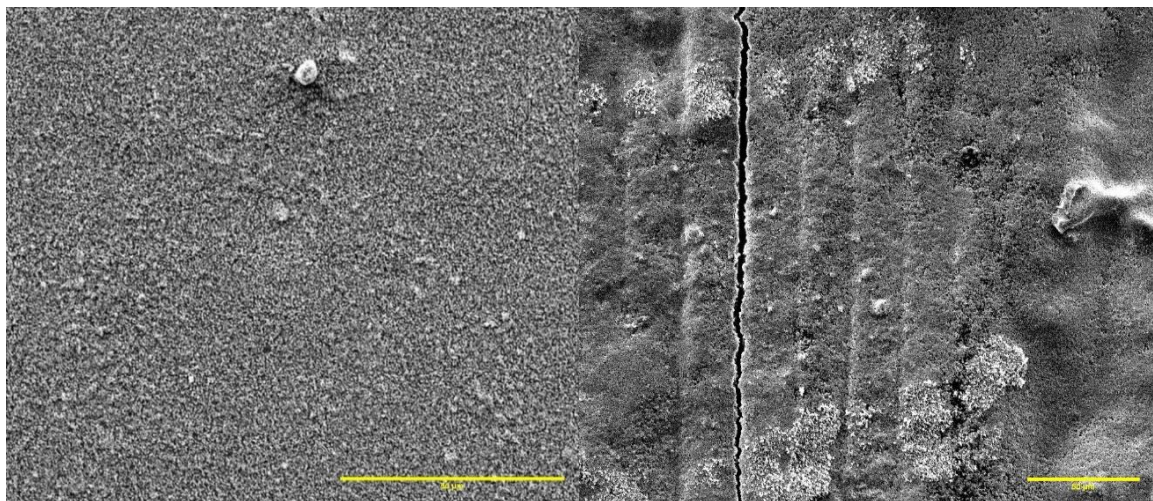


Figure 22: Tosoh TZ-8YS 42.5 vol% preconditioned parts, surface (left, 50 μm scale bar) and layer (right, 50 μm scale bar) all TZ-8YS slurries were made with MS13B Lithoz binder unless noted.

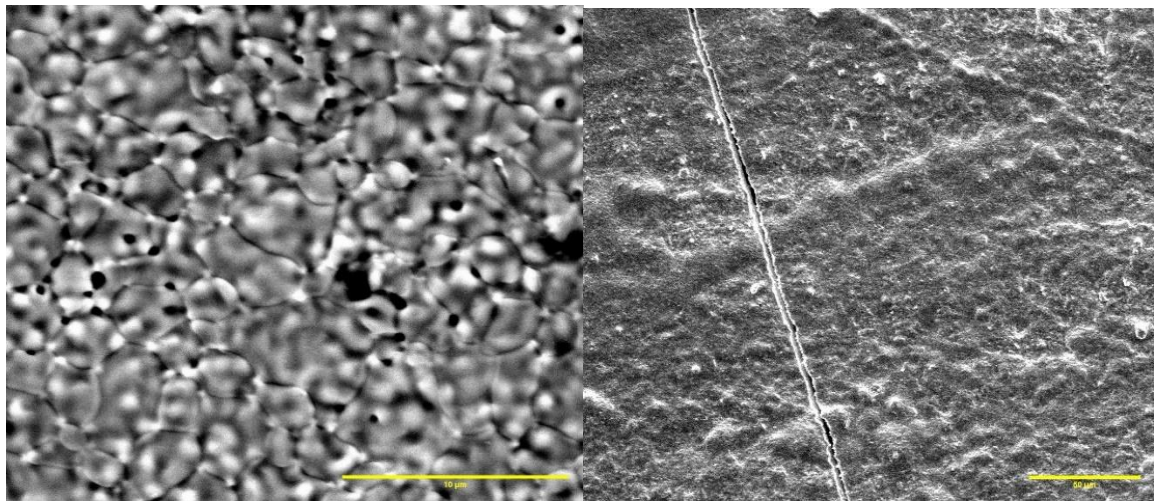


Figure 23: Tosoh TZ-8YS 42.5 vol% sintered parts, surface (left, 10 μm scale bar) and layer (right, 50 μm scale bar).

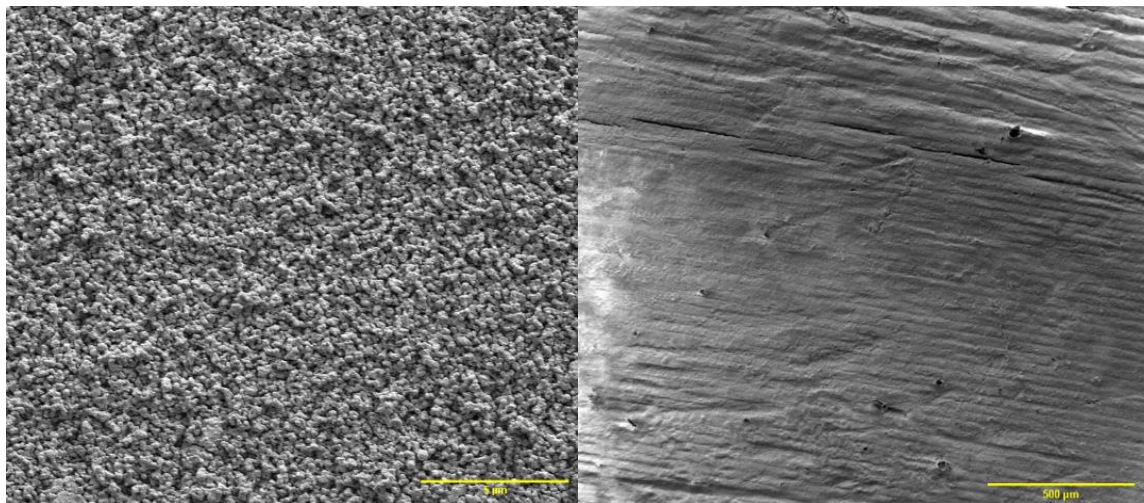


Figure 24: Tosoh TZ-8YS 45.5 vol% preconditioned parts, surface (left, 5 μm scale bar) and layer (right, 500 μm scale bar).

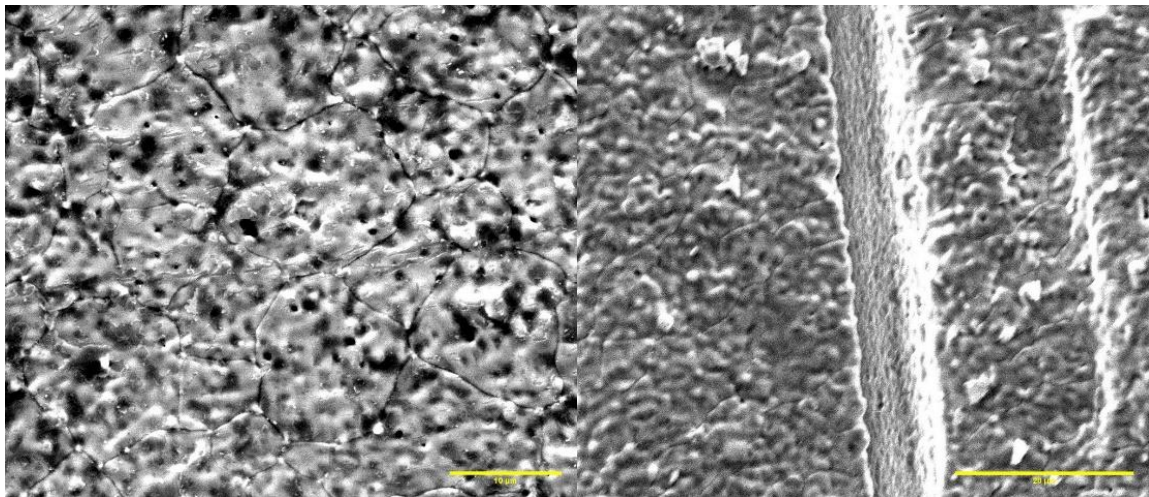


Figure 25: Tosoh TZ-8YS 45.5 vol% sintered parts, surface (left, 10 μm scale bar) and layer (right, 20 μm scale bar).

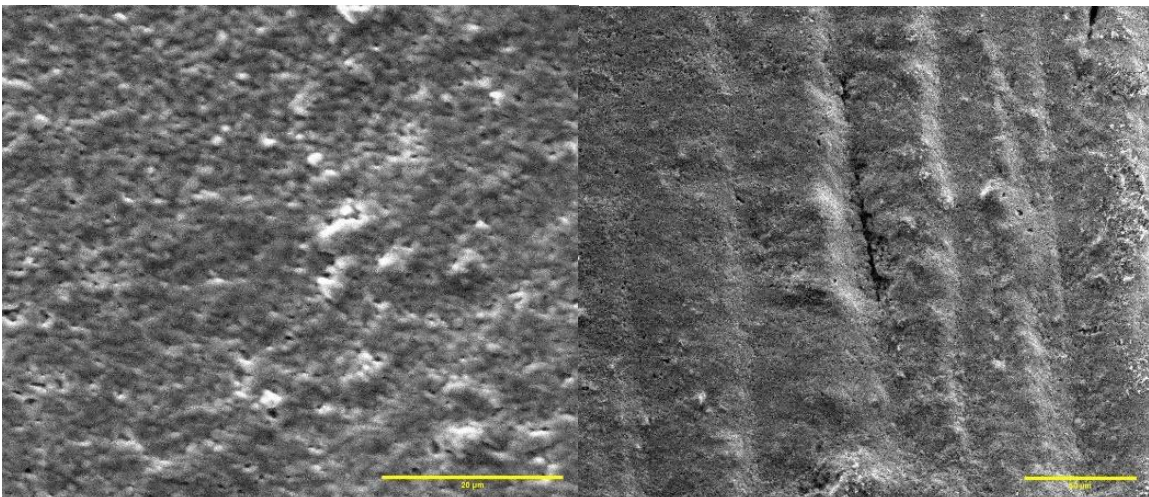


Figure 26: Tosoh TZ-8YS MS8 45.5 vol% preconditioned parts, surface (left, 20 μm scale bar) and layer (right, 50 μm scale bar).

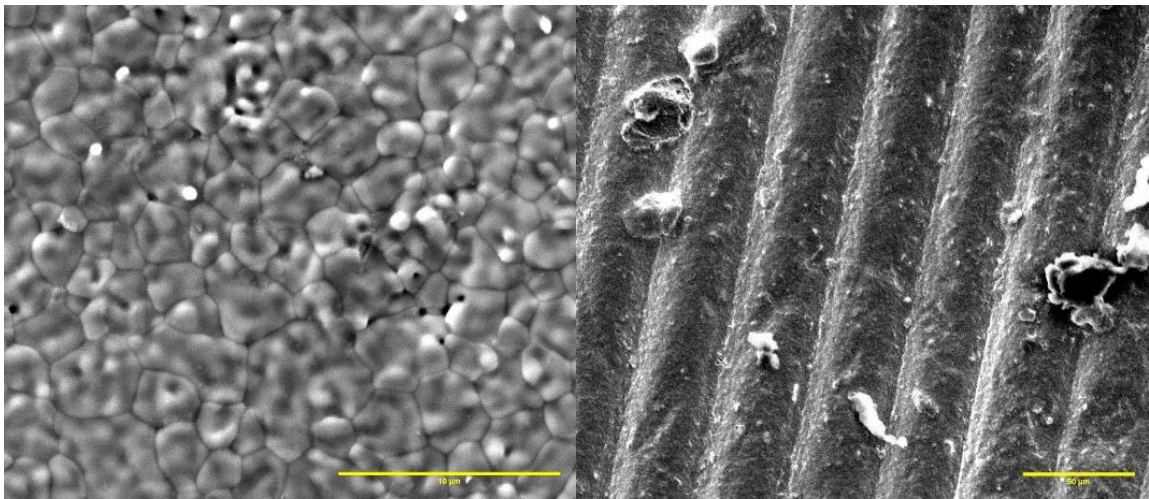


Figure 27: Tosoh TZ-8YS MS8 45.5 vol% sintered parts, surface (left, 10 μm scale bar) and layer (right, 50 μm scale bar).

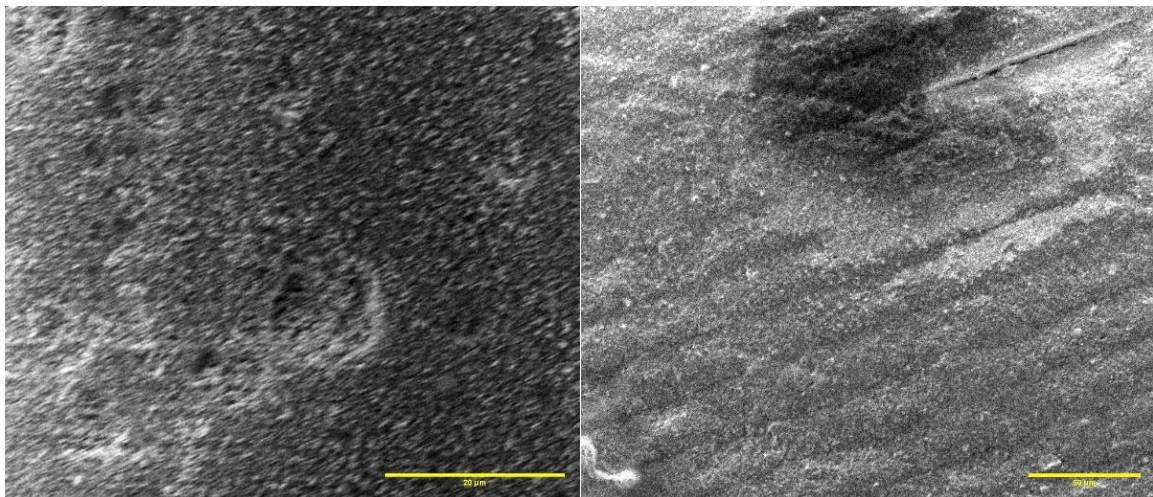


Figure 28: Tosoh TZ-8YS 46.5 vol% preconditioned parts, surface (left, 20 μm scale bar) and layer (right, 50 μm scale bar).

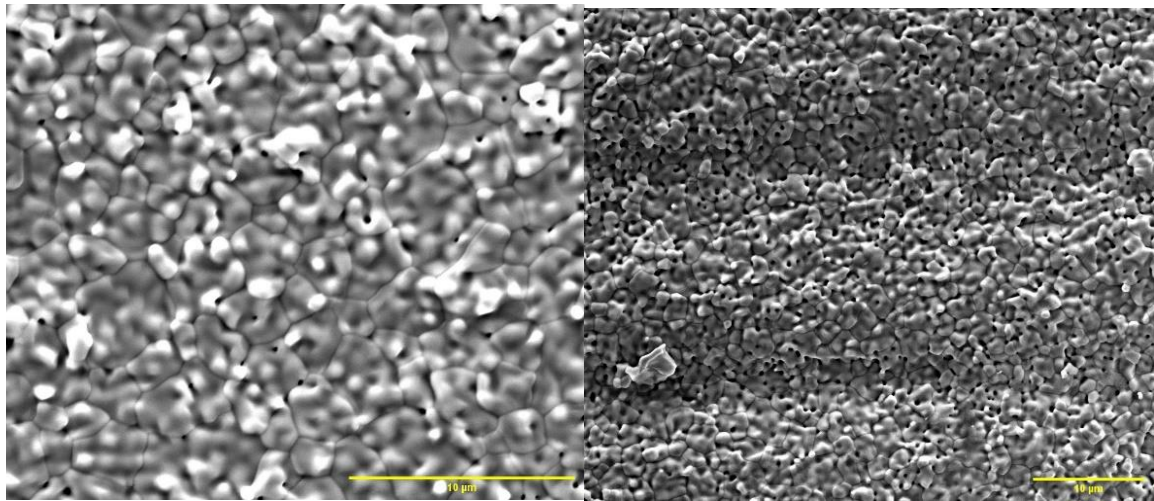


Figure 29: Tosoh TZ-8YS 46.5 vol% sintered parts, surface (left, 10 μm scale bar) and layer (right, 10 μm scale bar).

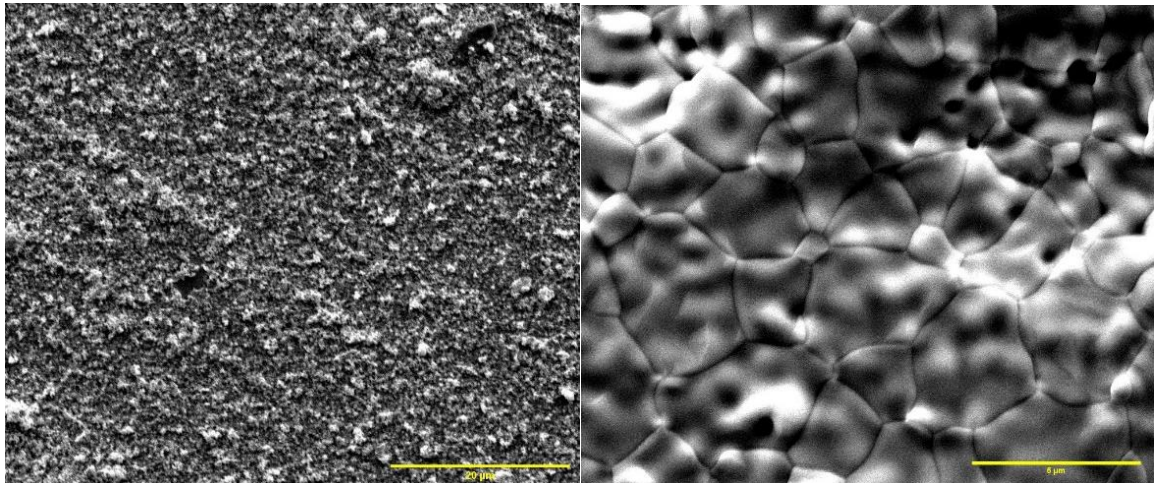


Figure 30: Tosoh TZ-8YS 48.5 vol% preconditioned part surface (left, 20 μm scale bar) and sintered part surface (right, 5 μm scale bar)

The Tosoh TZ-8Y powders had higher density and larger average grain size. The preconditioned powders were not as evident as the powders in the TZ-8YS samples. Figure 24 shows uniform distribution of the powders at 45.5 vol %. The preconditioned TZ-8Y samples like in Figures 31 and 33 show less uniform individual powder grains but more bunched powder and binder groups.

The sintered TZ-8Y parts had smaller features on the surface compared to the TZ-8YS parts. An example of the feature variation is the presence of small humps on the

visible grains' surface. The TZ-8YS grains had larger features compared to the smaller features seen on the surface of the TZ-8Y samples. The surface variation between the TZ-8YS and TZ-8Y parts shows some correlation between solid loading and particle sizes of the base powder. The TZ-8Y samples had larger grains with a slightly lower density of 93% vs 97% for the TZ-8YS samples.

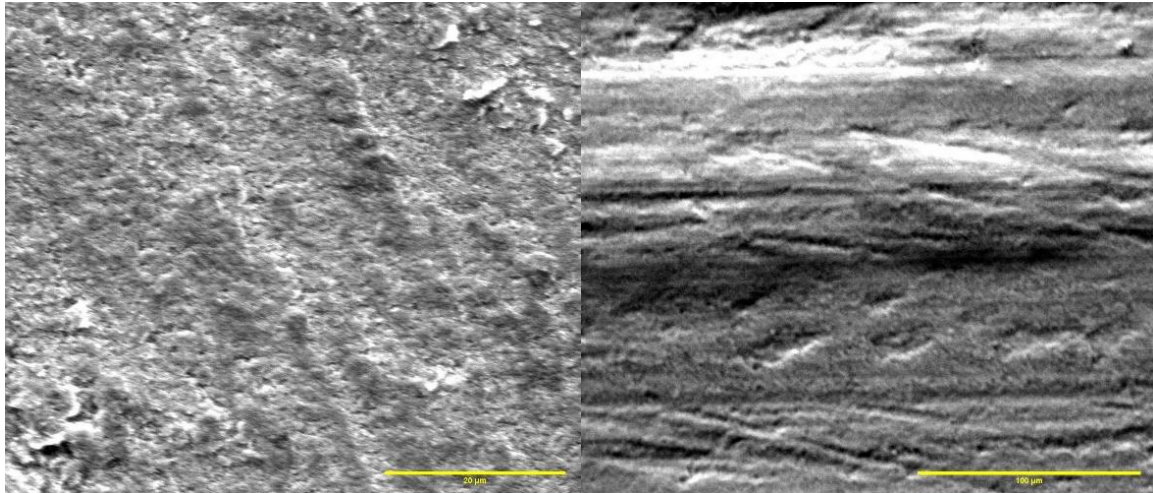


Figure 31: Tosoh TZ-8Y MS13B 40 vol % preconditioned parts, surface (left, 20 μm scale bar) and layer (right, 100 μm scale bar).

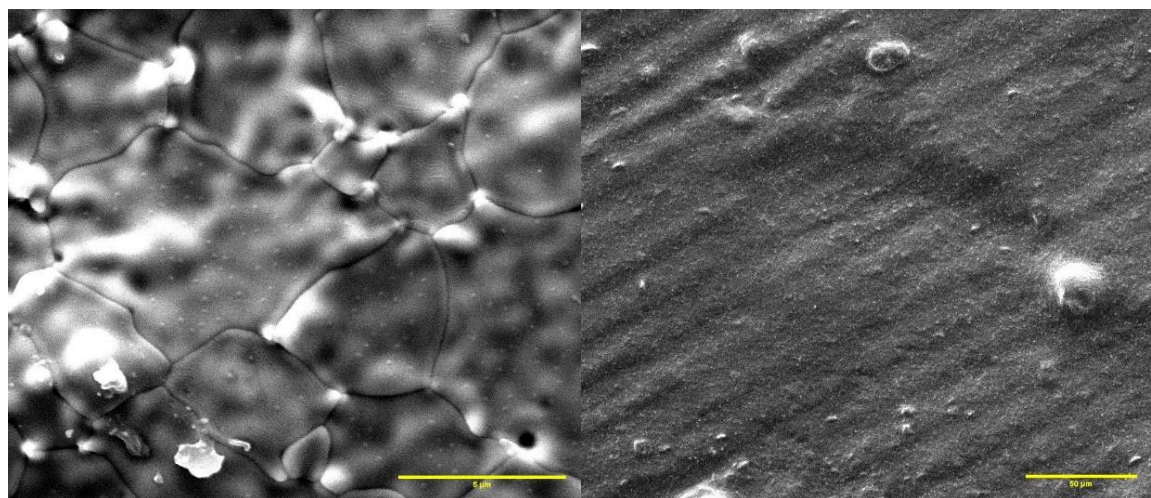


Figure 32: Tosoh TZ-8Y MS13B 40 vol % sintered parts, surface (left, 5 μm scale bar) and layer (right, 50 μm scale bar).

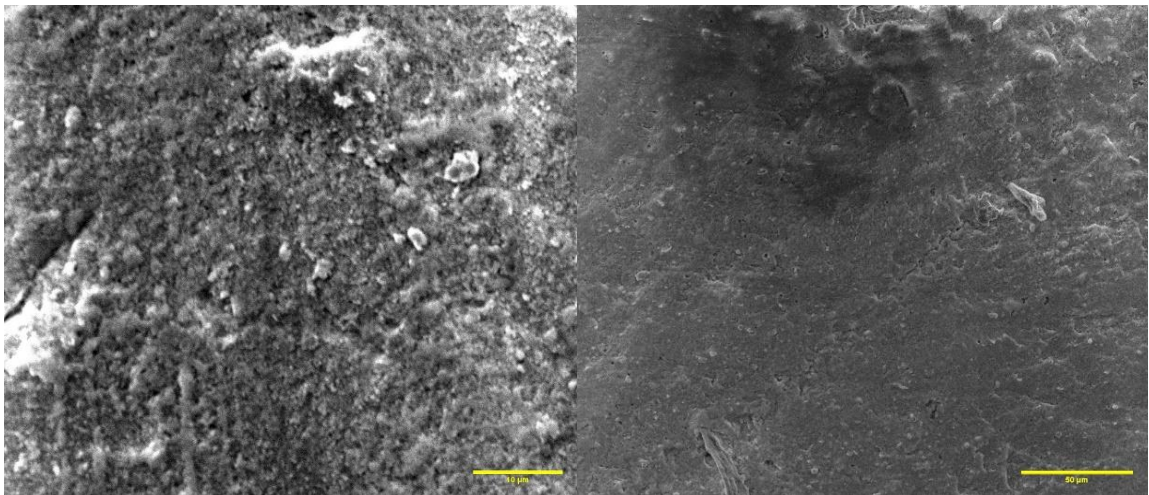


Figure 33: Tosoh TZ-8Y MS8 40 vol% preconditioned parts, surface (left, 10 μm scale bar) and layer (right, 50 μm scale bar).

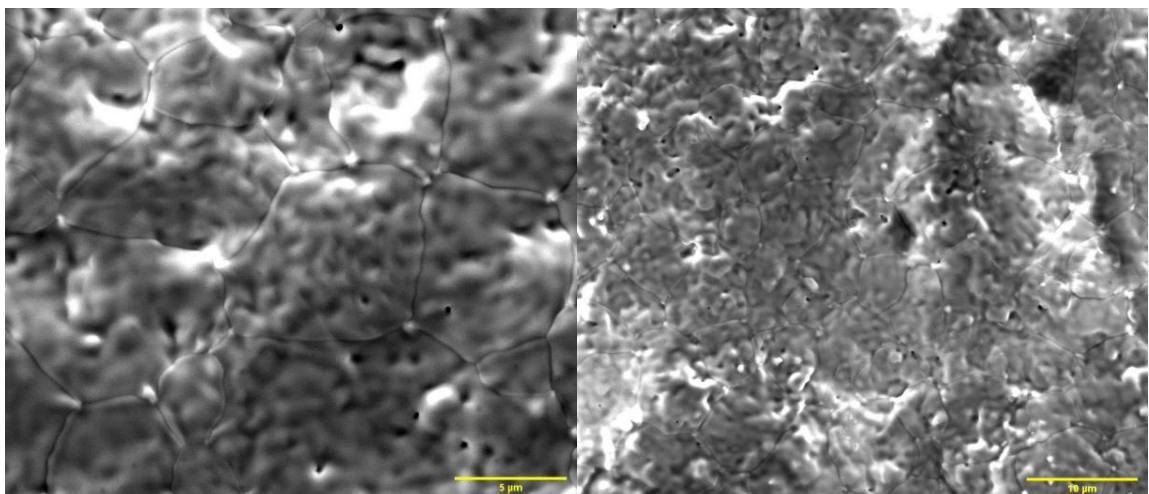


Figure 34: Tosoh TZ-8Y MS8 40 vol% sintered parts, surface (left, 5 μm scale bar) and layer (right, 10 μm scale bar).

3. Lithium Silicate

Lithium silicate (Li_4SiO_4) powder was made using the SSR method. The two reactants, lithium carbonate and silicon oxide, were mixed in different ratios to get the highest lithium silicate content. Five batches were made, but batch 4 and 5 were the same ratios. Once the powders had been mixed and calcined, the resulting material was a porous chalk like solid. Figure 35 shows the resulting solids, and the material maintained a shrunken shape of the crucibles used to calcine the powders. The left image in Figure 35 is the solid material on edge after heating, while the right, was the solid in a crucible after heating. Figure 36 shows the powders after they are ground down and sieved. The powders used to make MD-208 are smaller with an overall rounded shape. The powders to the left were used to make MD-203 and were much larger on average than those used for MD-208.

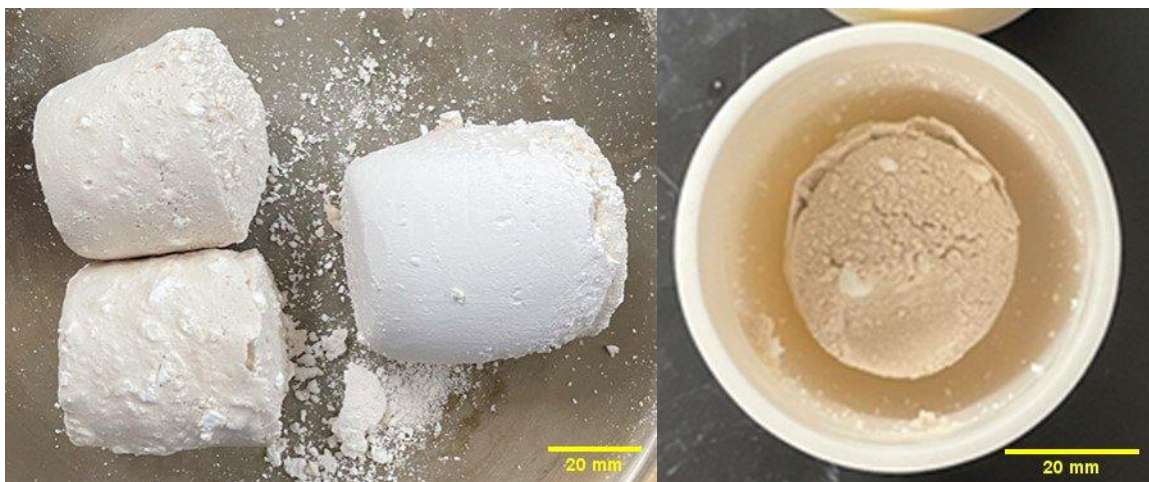


Figure 35: Lithium silicate batch five after calcining.

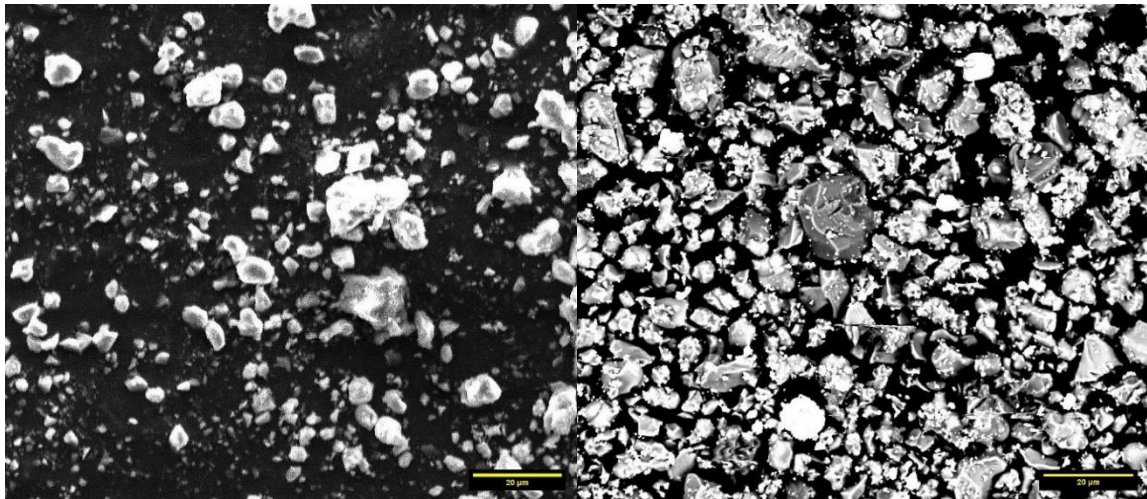


Figure 36: Lithium silicate powder, batch 5 (MD-208, left, 20 μm scale bar) and batch 1 (MD-203, right, 20 μm scale bar).

XRD was used to identify if Li_4SiO_4 successfully formed from the SSR. A comparison of the diffractograms from the different powder batches are shown in Figure 37. In batch one and three, peaks labeled with a triangle are Li_2SiO_3 PDF 00-029-0828⁰, caused by a lack of lithium carbonate (Li_2CO_3) present to supply lithium atoms to complete the transition to Li_4SiO_4 PDF 00-020-0637²⁰. In batch two, the diamond marked peaks revealed unused Li_2CO_3 PDF 04-010-7186⁰. The unreacted Li_2CO_3 and no SiO_2 PDF 00-046-1045²⁰. Batch four was used to test the results of a weight ratio of 5:2 Li_2CO_3 to SiO_2 . Batch five was a larger batch with the same ratio as batch four. Batch four was not enough powder to make a slurry therefore batch five was made. Figure 38 compares the powder's three diffractograms from batch five as a powder, as a presintered/as printed part, and a fully sintered part. The peaks in Figure 37 were labeled if they corresponded with a precursor material (Li_2SiO_3 , Li_2CO_3 , or SiO_2). The remaining unmarked peaks are for Li_4SiO_4 . In Figure 38, the peaks became sharper as the material transitioned from a powder to a sintered part. The final sintered part had sharper peaks with fewer small peaks from unreacted precursors in the material. The preconditioned part still has the binder used in printing. The amorphous binder is an acrylate monomer which produced the slight hump over 15-30° in Figure 38 on the center preconditioned

plot. The fully sintered part had sharp crystalline peaks at the corresponding Li_4SiO_4 peak angles.

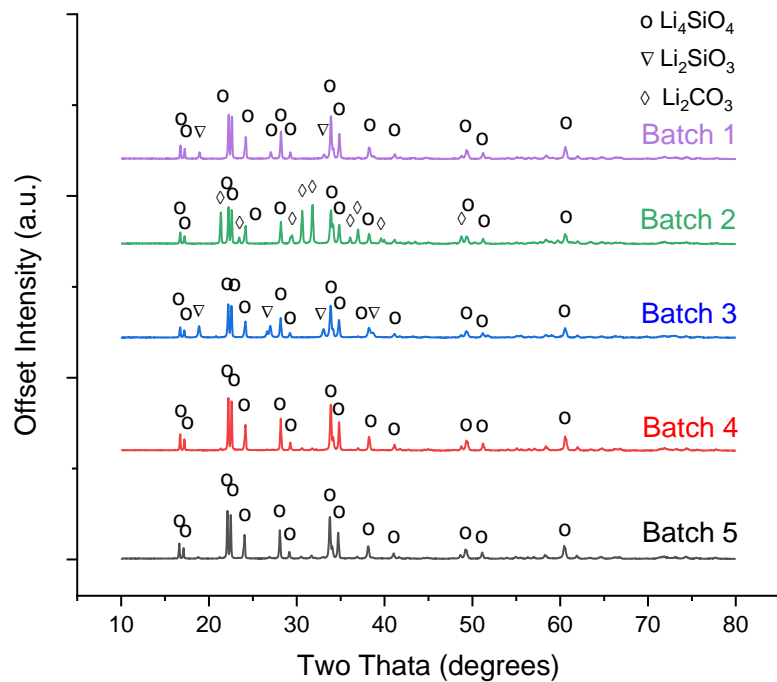


Figure 37: Lithium silicate Batch one to five powder XRD comparison, Li_4SiO_4 -PDF 00-020-0637²⁰, Li_2SiO_3 -PDF 00-029-0828²⁰, and Li_2CO_3 -PDF 04-010-7186²⁰.

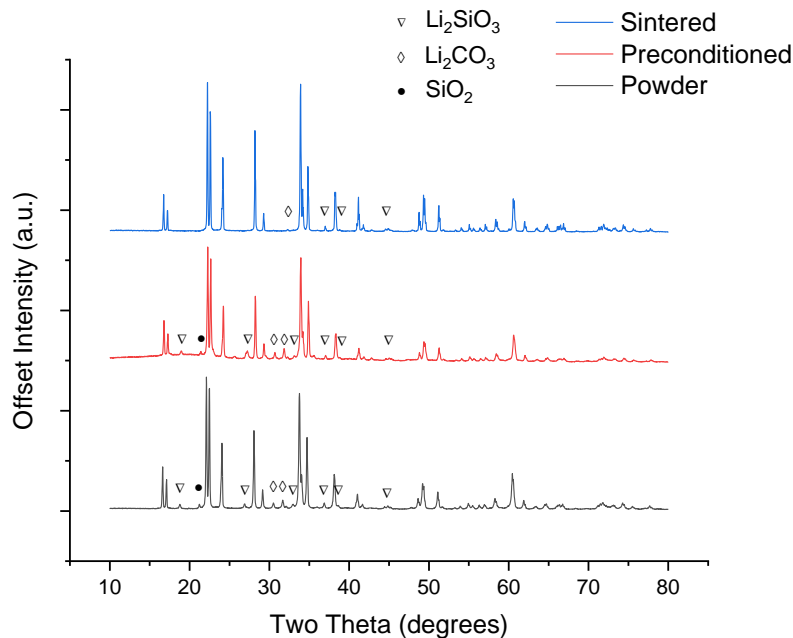


Figure 38: Printed lithium silicate part comparison from start to finish of batch 5, Li_2SiO_3 -PDF 00-029-0828²⁰, Li_2CO_3 -PDF 04-010-7186²⁰, and SiO_2 -PDF 00-046-1045²⁰ unmarked peaks are Li_4SiO_4 -PDF 00-020-0637²⁰.

Pressed lithium silicate powder from batch 5 was used to test the ideal sintering temperature for the printed parts. XRD diffraction was used to determine any structural changes caused by sintering. Three temperatures 800°C, 900°C, and 1150°C, were used for testing. The 800°C peaks had similar results to the starting powder with just slight peak sharpening. The results from the samples sintered at 900°C had sharper peaks than the 800°C samples. The 900°C samples also had minimal peaks from precursors remaining. The highest temperature tested was 1150°C which resulted in noticeable peak degradation, with peak broadening and intensity decreases compared to the 900°C samples results and PDF 00-020-0637²⁰. Figure 39 shows the peak variation for the three temperatures tested.

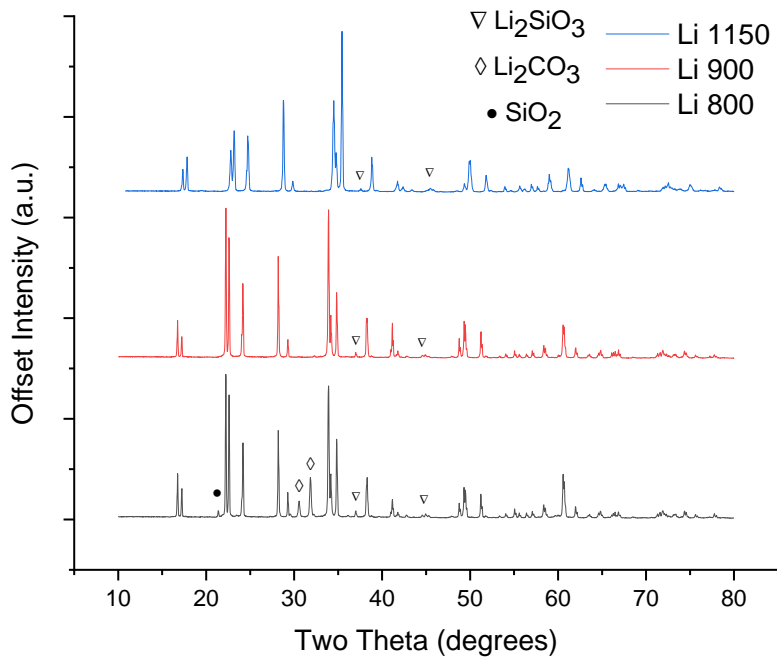


Figure 39: Lithium silicate sintering varied sintering temperature results. Peaks marked using Li_2SiO_3 -PDF 00-029-0828²⁰, Li_2CO_3 -PDF 04-010-7186²⁰, and SiO_2 -PDF 00-046-1045²⁰ unmarked peaks are Li_4SiO_4 -PDF 00-020-0637²⁰.

The lithium silicate slurry was printed initially using relatively thick layers at 100 μm as the lithium silicate slurry had relatively low light absorption, which allowed the light energy from the light source to penetrate deeper into the slurry. The 80 μm and 50 μm layers were also successfully printed with lower exposure energy. There was some partially cured slurry on the edges of parts that were not seen on the zirconia parts, and this was a result of light scattering in the slurry. The lithium silicate powder from batch five was used to make slurry batch number MD-208, which resulted in successfully printed parts. Slurry batch MD-203 was made from powder from batch 1. However, the slurry sat for two weeks after being made. The initial dispersion was promising however the suspension became too viscous to spread in the printer vat, so it was not printable and had to be discarded. Figure 40 is the slurry from MD-203 in the vat sticking to a spoon. A typical slurry flows off with relative ease. TABLE VI shows the slurry batch number, powder, binder, and solid loading of the two prepared slurries. The only successful prints used the MD-208 slurry.



Figure 40: Lithium silicate MD-203 slurry in printer deemed too thick.

TABLE VI: Lithium silicate slurries.

Lithoz Batch Number	Powder	Binder	Solid Loading (Vol%)
MD-203	Lithium Silicate	MS13B	47%
MD-208	Lithium Silicate	MS13B	51%

The powders used to make slurry MD-208 were sieved through a 45 μm mesh which still resulted in larger than standard particles for printable slurries. The YSZ test slurries had an average particle size below one μm . The large particle size of the lithium silicate resulted in a relatively abrasive slurry. Light penetration was quite high leading to light scattering, which caused some partial curing around the parts' edges. The larger particles also caused weird flow properties in the slurry. The blade speed for spreading the slurry needed to be closely monitored because the slurry would not spread well if

speeds were too high or enough time was not given to fill gaps. However, the slurry had little resistance against the blade; in other slurries that had proven difficult to print, the slurry became too viscous and sticky for the blade to spread and would put too much pressure on the blade causing it to abort. The larger particle size and solid loading of 51% resulted in the printed parts being relatively weak compared to similar YSZ parts. The high solids content led to less binder in the slurry which resulted in weakly bound parts. The material was easily removed from the body of the part. Parts were printed with three different layer heights 100 μm , 80 μm , and 50 μm . The 50 μm layer parts resulted in a small dimple in the center, which is typically seen in printed parts of low layer thickness high viscosity slurry parts. This is because the material is pulled down from the center with the build plate raises after each layer. As the part is printed, the dimple slowly grows with each additional layer. In Figure 41, the two largest disks to the left have small surface dimples. When looking at Figure 41, the impression of the vat's parts to the right shows how poorly the light penetrates directly through the slurry to bind the new layer to the previous layers. The poor binding also resulted in weaker parts as the powders were poorly bonded by the binder.

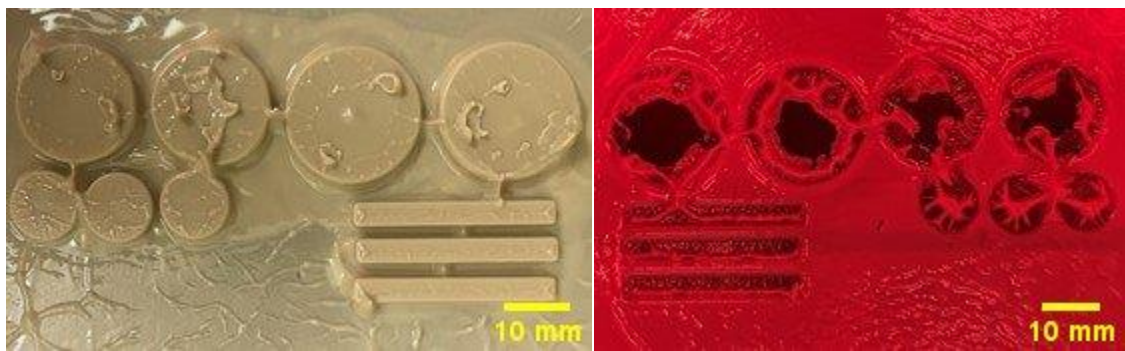


Figure 41: MD-208 lithium silicate, parts (left) and slurry impression in the vat after (right).

Once cleaned, the parts had no visible cracking or flaking; however, there were some pinholes on larger samples. During cleaning, the samples had partially cured residue on the edges of the parts. The binder's weak bonding allowed for the sharp edges of samples to become rounded over during cleaning. Overall, the parts stayed intact with no significant flaws, difficulty removing from the build plate, or difficulties cleaning.

Figure 42 has examples of cleaned samples before being placed in the oven for preconditioning. The image to the right of Figure 42 was lit from the yellow lighting in the Lithoz cleaning station. The yellow light helps keep excess slurry on parts uncured. Also, in Figure 42, the large disk to the front of the right image has signs of small pinholes.

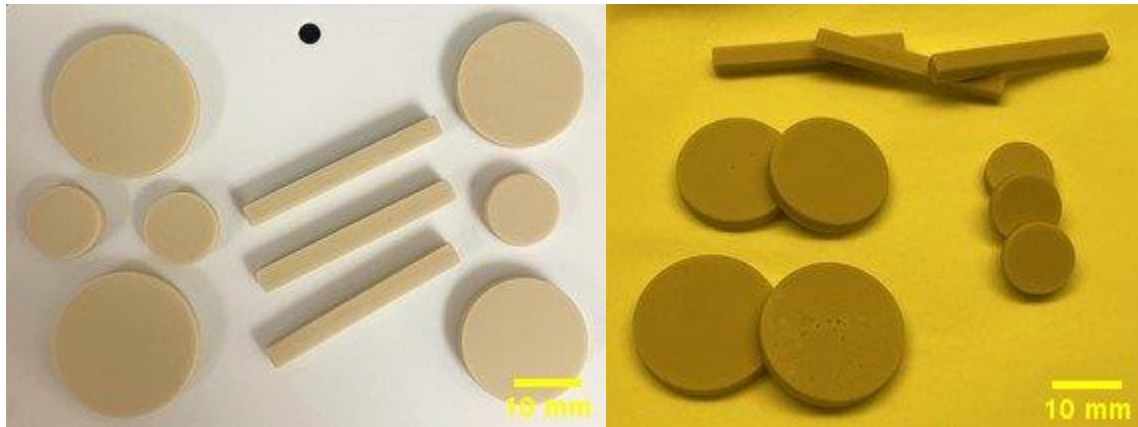


Figure 42: MD-208 lithium silicate parts cleaned before preconditioning (both 10 mm scale bars).

The test parts preconditioned well; no surface cracks were visible. Figure 43 shows both the surface and layer view of a preconditioned sample. No layer was visible, with large particles visible and little space evident for the binder, resulting from the high solid loading. Powder could still be easily removed from the preconditioned samples' surface after being heated for three days.

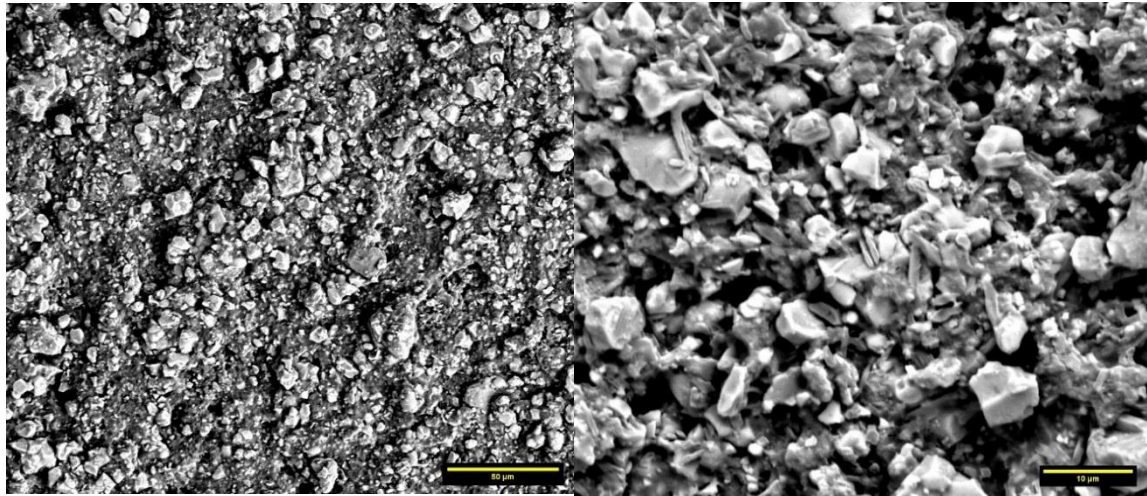


Figure 43: MD-208 lithium silicate part preconditioned, surface (left, 50 μm scale bar) and layer (right, 10 μm scale bar).

Five different sintering profiles were tested, ranging from seven to eight steps, as shown in TABLE III. The initial five steps warmed the parts and cured the binder. The sixth step was the burnout point for the binder. The initial steps had a slow ramp rate to avoid cracks by raising the temperature too quickly. The first, second, and third profiles had only seven steps, with the final step being the temperature at which the parts would sinter. Sintering temperature and dwell times were varied over a narrow range to improve density in the final parts. The fourth and fifth profiles included a step between binder burn out and sintering to heat any unreacted precursors in the material.

TABLE III: Lithium silicate sintering profiles (* Not Included in Profile).

Temperature (°C)	Ramp (°C/min)	Dwell (h) Profile 1	Dwell (h) Profile 2	Dwell (h) Profile 3	Dwell (h) Profile 4	Dwell (h) Profile 5
130	0.1	3	3	3	3	3
170	0.1	3	3	3	3	3
220	0.1	4	4	4	4	4
250	0.2	5	5	5	5	5
325	0.2	5	5	5	5	5
430	0.5	2	5	5	5	5
680	1	*	*	*	*	5
700	1	*	*	*	5	*
800	1	*	*	5	*	5
900	1	4	5	*	5	*
120	Naturally Cooled	Naturally Cooled	Naturally Cooled	Naturally Cooled	Naturally Cooled	Naturally Cooled

Once sintered, samples printed with the layer perpendicular to the disk's large face had noticeably less bubbling occurred on the samples' surface. The larger surface area between layers led to more bubbling on the surface, as shown in Figure 44, which was sintered at 900 °C. Bubbling can be seen on the large round disk with no noticeable bubbling on either smaller disks' surface. The smaller, fully round disk had the same layer orientation as the larger disk. The larger the overall sample, the worse the bubbling as seen in Figures 44 and 45. The samples shown in Figure 45 were the two densest parts sintered at ~ 90% of theoretical density. Those are the two disks with the small foot were printed, so the layers were perpendicular to the disk face. All the samples had signs of bubbling on the surface; however, the samples with the smaller surface area layers had much less, with only the side facing up during sintering developing surface bubbles. The samples in Figure 45 were sintered at a lower temperature of 800°C. The samples sintered using profiles 4 and 5 had noticeably more surface bubbles than the first three profiles tested. The difference being the fourth and fifth profiles had an additional segment added in. The segment held at temperatures in the SSR range used to make the samples' powder base before ramping to a final sintering temperature. The additional step was to provide more time for the samples at an elevated temperature to react, causing off-gassing of CO₂ from the leftover precursors used in SSR. The CO₂ is believed to cause the bubbling, which primarily affects the sample's side facing away from the surface the sample is resting on.



Figure 44: Sintered lithium silicate from sintering profile four front (left) and back (right).

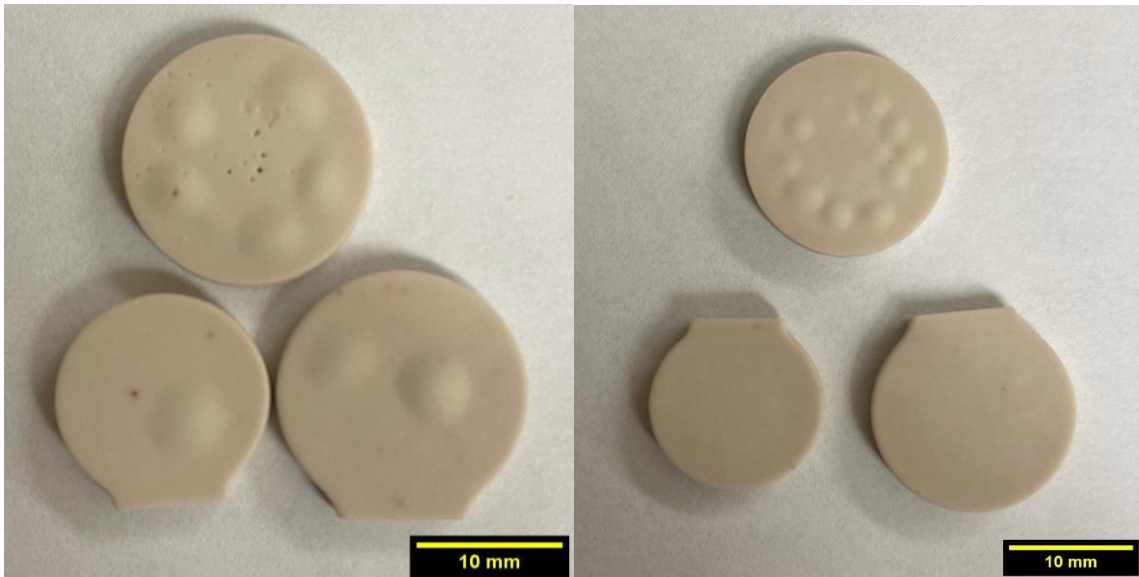


Figure 45: Sintered lithium silicate from sintering profile five front (left) and back (right).

The sintering profiles were adjusted to improve bulk density and average grain size. TABLE VII shows how these adjustments affected density and grain size. The dwell for debinding, sintering temperature, and dwell, and later a reaction temperature and dwell were altered to improve density and grain size. The last profile had the best results for density with an average of 87%, and the maximum for a specific sample was 90%. The samples with a lower surface area between layers relative to size resulted in the best density. Samples that went to higher sintering temperatures of 900°C resulted in larger grain sizes, as seen in profiles 1, 2, and 4, where 3 and 5 sintered at 800°C. Profiles 4 and 5 with an addition of a reaction temperature step showed improved density and grain size.

TABLE VII: Lithium Silicate Density and Grain Size.

	Profile 1	Profile 2	Profile 3	Profile 4	Profile 5
Average Density	84%	78%	84%	85%	87%
Average Grain Size (GS)	35 μm	27 μm	18 μm	42 μm	22 μm
GS Standard Deviation	15+/- μm	11+/- μm	9+/- μm	20+/- μm	8+/- μm

When the first three profiles were tested, poor uniform grain growth was evident. The alterations to the sintering temperature and debinding dwell had minimal effect. Profile 4 and 5 included a reaction step used to react any carbonates remaining in the material. The result improved density and grain growth. Figures 46-48 correspond to the first three profiles and show pinholes or an open structure.

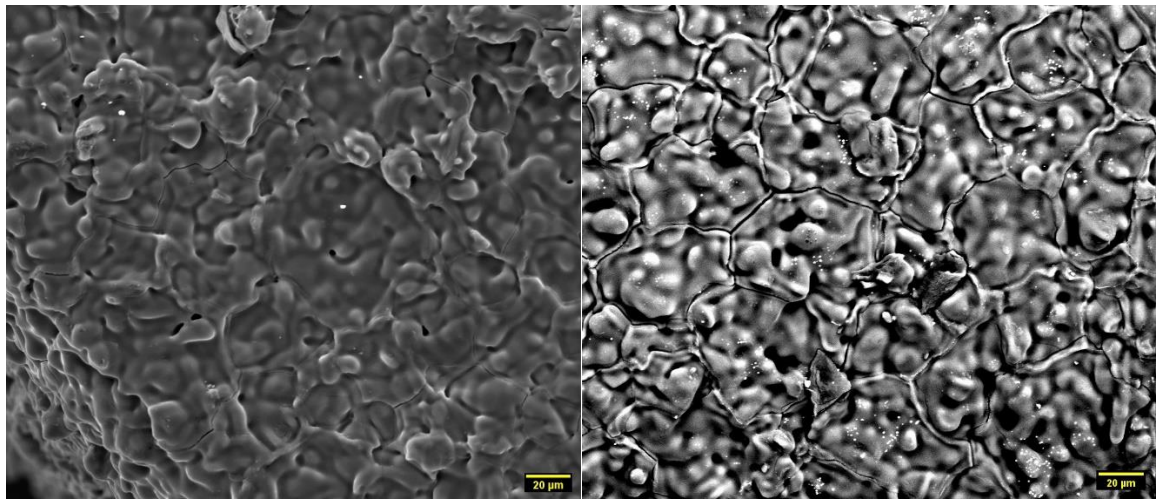


Figure 46: Lithium silicate sintered part profile one, surface (left, 20 μm scale bar), and layer (right, 20 μm scale bar).

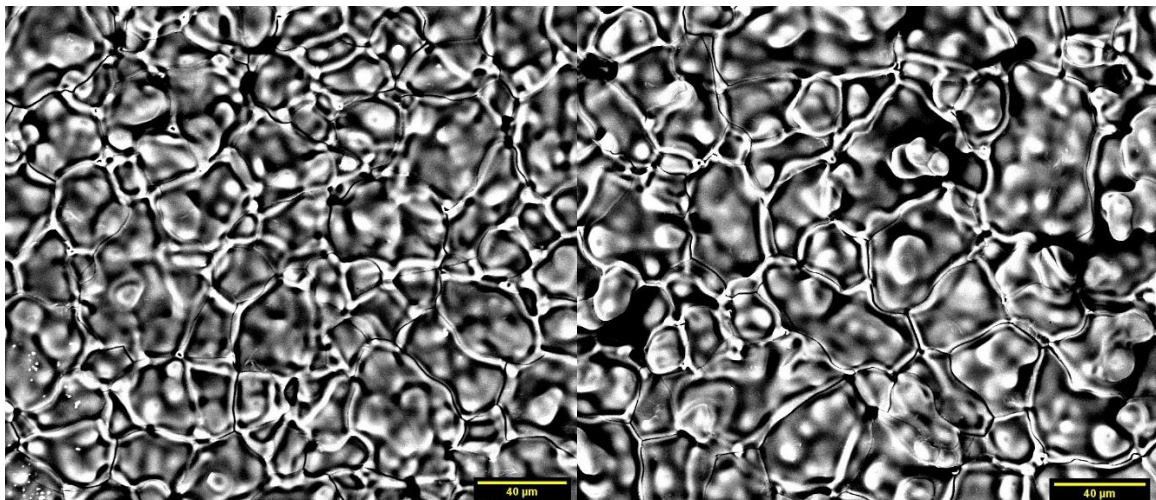


Figure 47: Lithium Silicate sintered part profile two, surface (left, 40 μm scale bar) and layer (right, 40 μm scale bar).

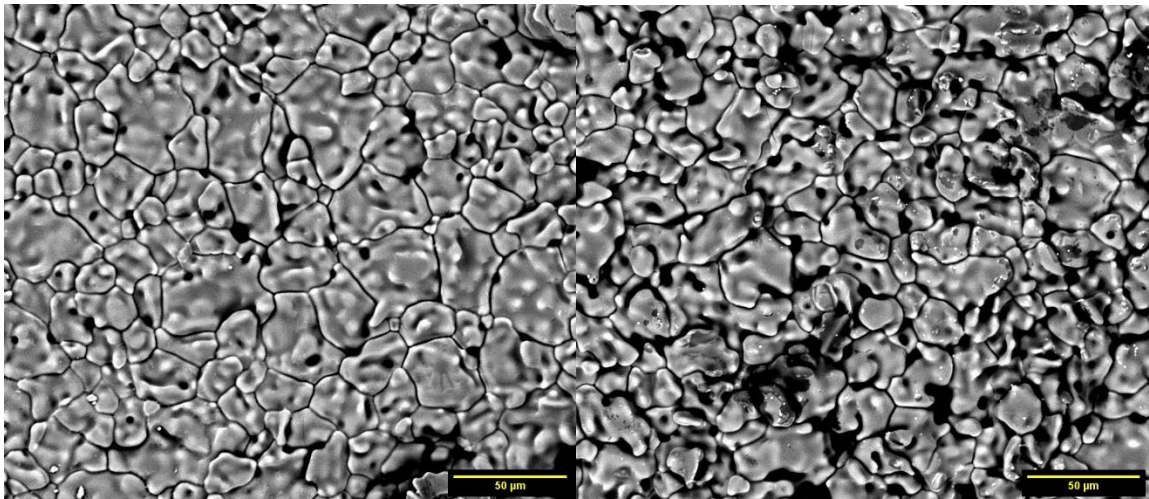


Figure 48: Lithium silicate sintered part profile three, surface (left, 50 μm scale bar) and layer (right, 50 μm scale bar).

Figures 49 and 50 are the last two profiles that have improved grain growth and density. Figure 49 shows tightly packed grains with an average grain size of 42 μm . The left image in Figure 50 is the surface of a disk that was printed parallel to the build plate, with an average density of 86%, where the image to the right is the layered side of a disk printed perpendicular to the build plate with an average density of 90%. The images to the right of Figures 46-50 are all layered surfaces; bubbles typically affected non-layered surfaces. The materials' layers helped release CO₂ gas from the lithium carbonate through lithium silicate reaction during sintering; this is evident because samples with lower layer surface area had higher density, and more open pores can be seen on a layered surface like seen in the Figures 46-50.

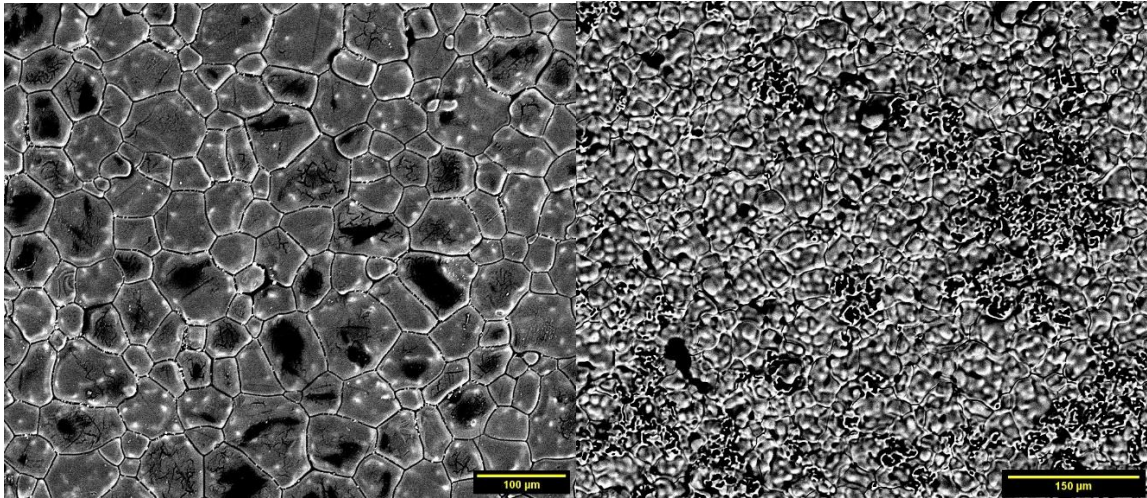


Figure 49: Lithium silicate sintered part profile four, surface (left, 100 μm scale bar) and layer (right, 150 μm scale bar).

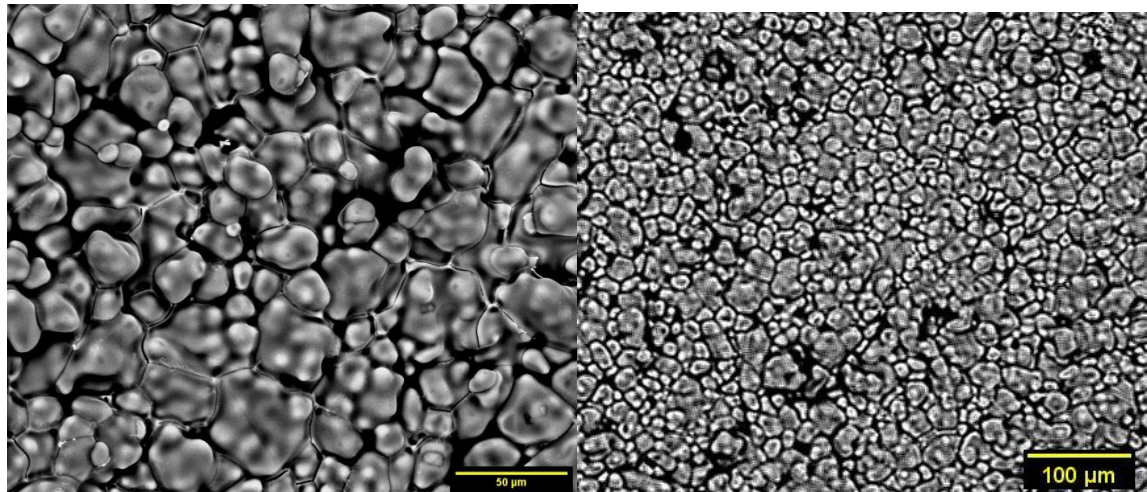


Figure 50: Lithium silicate sintered part profile five, surface (left, 50 μm scale bar) and layer (right, 100 μm scale bar).

4. Electrical Conductivity

Impedance spectroscopy was used to find the activation energy of 3D-printed YSZ and lithium silicate samples. The samples were printed as 10mm x 3mm disk. Figure 51 shows samples after testing. The discoloration resulted from heating the gold electrode during impedance measurements. The three parts at the top of Figure 51 are the "layered" samples where the printed layer orientation is perpendicular to the electrodes as

shown in Figure 5. The three parts at the bottom of Figure 51 are the "surface" samples where the layer orientation is parallel to the electrodes also shown in Figure 5.



Figure 51: Gold-coated lithium silicate (left), Tosoh TZ-8Y (middle), and Tosoh TZ-8YS (right) samples after impedance testing.

Samples were placed into a furnace programmed to follow a heating cycle of 100°C to 800°C at 50°C increments for YSZ and 100°C to 300°C at 25°C increments for lithium silicate. Platinum leads were placed on the top and bottom of the sample disk, contacting the electrodes on both the top and bottom. The platinum leads were connected to the impedance analyzer. Figure 52 shows interior set up of the impedance test rig before being closed. An alumina rod was used as a weight to hold the platinum leads against the electrodes on the samples.



Figure 52: Lithium silicate test sample in furnace with impedance test leads.

Once the samples had undergone impedance testing the bulk resistance was determined using a semicircle fit. The data collected was plotted in ZView with half circles fitted to the first curve which was representative of the bulk resistance. Figure 53 shows an example of data fitted from a lithium silicate sample. The resulting bulk resistance (R_b) was used to find the bulk conductivity of the material calculated using (2)^{12, 22}.

$$R_b = \frac{1}{\sigma_b A} \rightarrow \sigma_b = \frac{d}{AR_b} \quad (2)$$

where d is the thickness of the disk tested (distance between the electrodes), A is the surface area of the electrode contacting the sample or face of the disk, and R_b is the bulk resistance. Evident of contributions from grain boundaries and the electrode interface seen in Figure 54. The first fitted curve being the bulk resistance and the rest of the curves represent the grain boundary and electrode interface resistance. Ideally, an additional contribution from the layered structures to the impedance data is expected. In order to confirm such a contribution, more systematic study varying layer thickness and detailed impedance data with equivalent circuit analysis will be needed.

The bulk conductivity was then used to generate Arrhenius plots, which were used to find the activation energy of the printed parts. The log of the bulk conductivity was calculated and plotted as a function of the inverse of the absolute temperature. The

slope of a linear best fit line was used to find the activation energy. The Arrhenius equation (3)^{22, 23} was used to find the activation energy for the two materials.

$$k = A e^{-E_a/RT} \rightarrow \ln k = -\frac{E_a}{RT} + \ln A \rightarrow y = mx + b \quad (3)$$

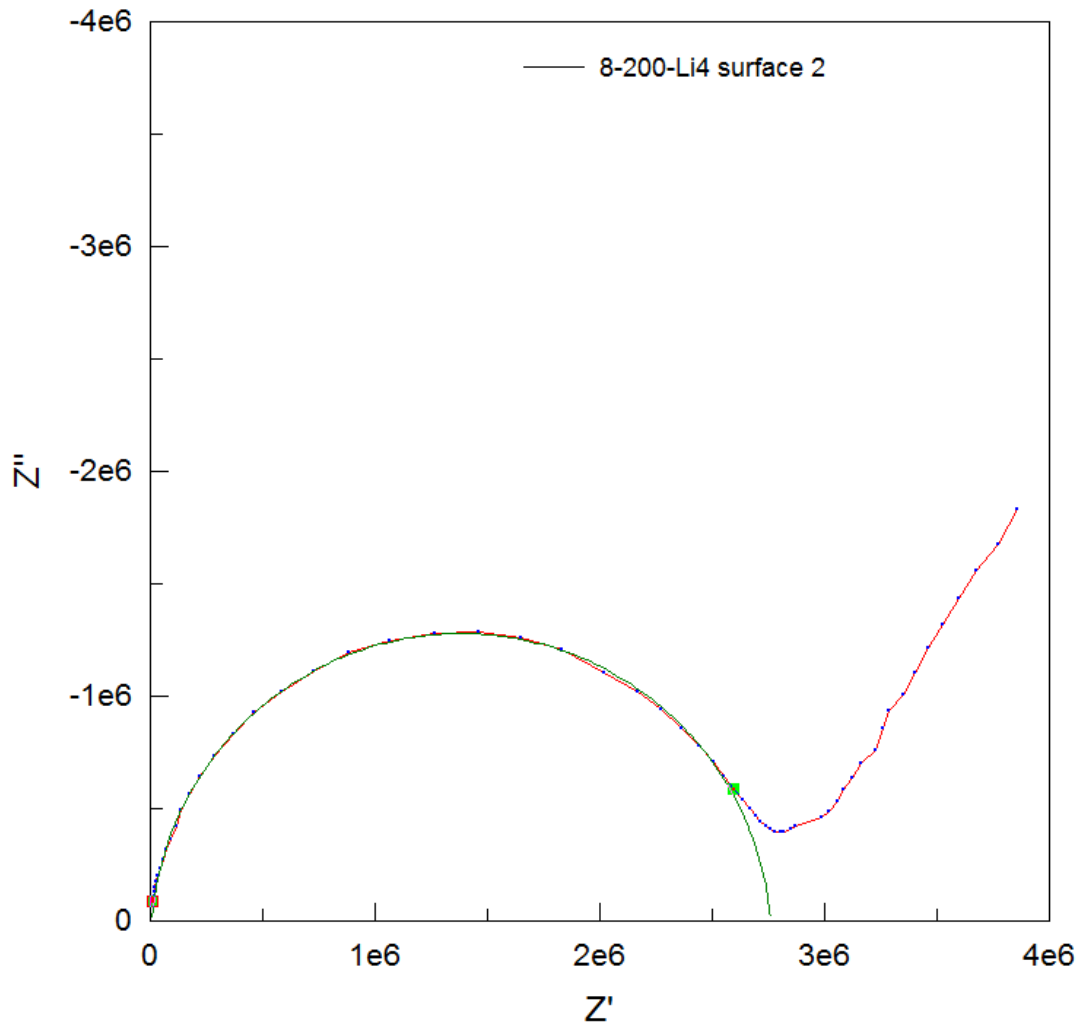


Figure 53: Lithium silicate surface at 200°C with bulk and grain boundary resistance curve fit.

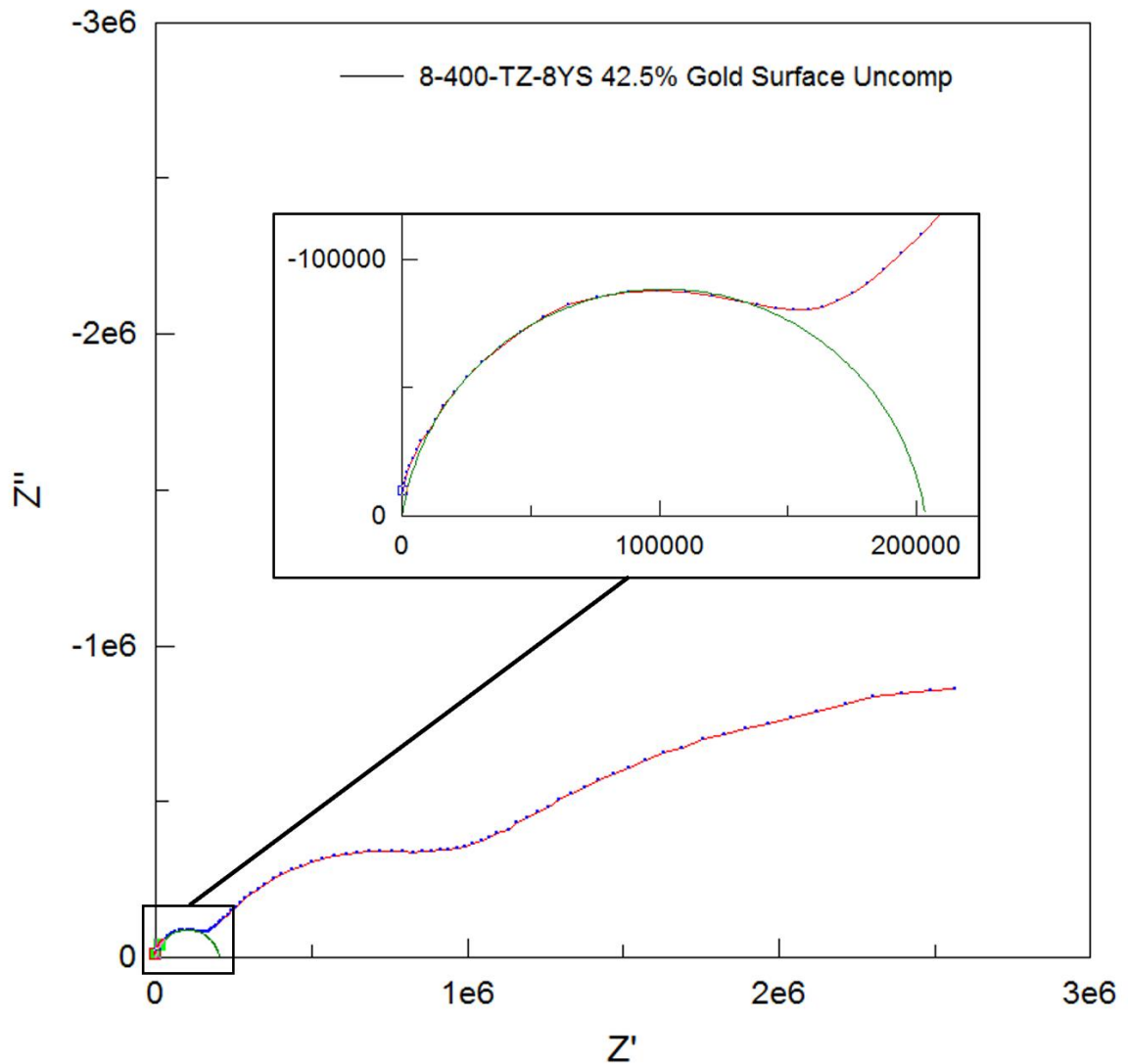


Figure 54: YSZ surface at 400 °C bulk and grain boundary resistance curve fit.

Key features tested were layer orientation to determine if there were any effects on the conductivity and activation energy of the material. AM YSZ samples resulted in a bulk conductivity average of $1.33 \times 10^{-3} \Omega\text{-cm}$ at 300 °C. AM lithium silicate samples resulted in an average bulk conductivity value of $5.14 \times 10^{-5} \text{ S cm}^{-1}$ at 300 °C compared to Adnan *et al.*¹² who reported conductivity value of $1.16 \times 10^{-4} \text{ S cm}^{-1}$ at 100 °C. The conductivity values were less for the AM parts compared to monolithic parts.

TABLE VIII. is a comparison of the bulk experimental averages found in the literature. The bulk activation energy for both lithium silicate layer orientations resulted

in 0.22 eV. However, the surface orientation had slightly higher bulk resistance values compared to the layered orientation. The same bulk resistance variation was also observed in the YSZ samples with slightly higher resistance values for surface orientation samples compared to layer orientation samples. The bulk activation energy for the two YSZ compositions had a 0.1 eV difference. With the samples grained TZ-8Y having the higher activation energy. Both YSZ and lithium silicate materials demonstrated no significant direct effect on electrical properties caused by varying layer orientation during printing and electrode placement.

TABLE VIII: Bulk Activation energy experimental values vs literature values.

	Experimental Average	Experimental Range	Literature Average	Literature Range
Lithium Silicate	0.22 eV	0	0.19 eV	0
YSZ (TZ-8Y)	0.39 eV	0.01	1.16 eV	0.18
YSZ (TZ-8YS)	0.29 eV	0.01	1.16 eV	0.18

Figures 55 and 56 show the Arrhenius plots for both lithium silicate and YSZ. The average calculated bulk activation energy for YSZ was 0.34 eV and the average for lithium silicate was 0.22 eV. Figures 55 and 56 also show the Arrhenius plots for average grain boundary activation energy for both YSZ and lithium silicate. The grain boundary activation energy for the YSZ was 0.48 eV and 0.40 eV for lithium silicate. Both materials had consistently higher grain boundary activation energies than bulk activation energy.

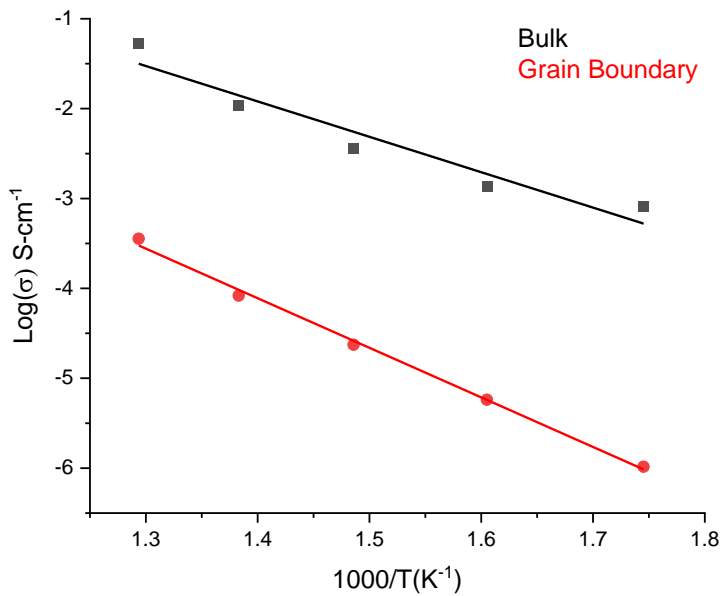


Figure 55: Arrhenius plot for Tosoh YSZ samples bulk and grain boundary activation energy.

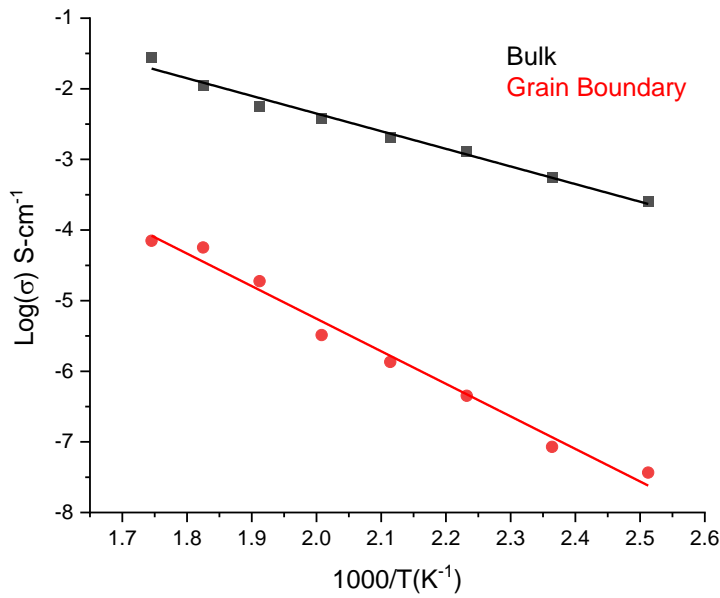


Figure 56: Arrhenius plot for lithium silicate samples bulk and grain boundary activation energy.

Lithium silicate experimental activation energy was determined for a temperature range of 125-300 °C with a printed layer thickness of 100 µm. A 100 µm layer thickness is relatively high compared to typical LCM layers. The experimental average bulk activation energy for lithium silicate was 0.22 eV. The lowest recorded bulk activation energy found was from Adnan *et al.*¹², which was 0.19 eV for samples prepared by sol-gel and pressed into pellets and sintered. The 3D-printed lithium silicate samples had high porosity with an average density of roughly 85% as well as large outgassing from unreacted precursors creating large scale dysconnectivity and defects in the materials, thus increasing the activation energy.

YSZ experimental activation energy was determined for a temperature range from 300°C to 500°C with a printed layer thickness of 25 µm. The experimental average bulk activation energy was 0.34 eV with Kwon *et al.*²⁴, report bulk activation energies of 1.16 eV. The lower activation energy for the experimental 3D-printed and sintered material may be attributed to electrons potentially finding a path of least resistance not found in traditionally formed parts. The layering may lead to micro cracks in the bulk material as well as uneven sintering leading to stresses in individual layers also causing delamination. The thermal profile does not separate debinding from sintering combining both processes into one. Debinding may be causing tunneling in the microstructure from the escaping binder gases with sintering following leading to a nontraditional microstructure.

IV. SUMMARY AND CONCLUSIONS

This work was an early attempt at utilizing LCM technology to produce 3D-printed and sintered samples made from YSZ and lithium silicate. The work also drew attention to the layered microstructure's potential effects on the 3D-printed materials' bulk conductivity and activation energy.

Five YSZ powders with three binder systems were tested at varying solids loading percentages. Two powders, the Tosoh TZ-8YS and TZ-8Y, along with the Lithoz MS13B and MS8 binders, resulted in printable slurries. Seven total variations were successfully printed and sintered. The TZ-8YS powders with a solid loading of 45.5-46.5 % matched with MS13B binder were determined to be the ideal slurry for 8 mol % YSZ.

Five batches of lithium silicate powder were made, resulting in two lithium silicate slurries. The binder used was Lithoz MS13B. The slurry formulations resulted in high curing depths and solid loading amounts. However, the slurry would cure when mixed, so working times were limited to a week. One lithium silicate slurry was successfully printed and sintered. The slurry contained 51% solid loading and MS13B binder.

Impedance spectroscopy was used to determine the effects layering and orientation of printed layers to test electrodes may have. Samples printed with different layer orientations were tested to determine any significant bulk conductivity variations and activation energy variations. There was no direct evidence of the layer orientation having significant effects on the bulk conductivity and activation energies of tested samples.

These results demonstrate that these materials can be successfully 3D-printed and sintered to dense products. Preliminary characterization was used to determine how effectively parts could be printed. Micro surface cracking, surface bubbling, and activation energies for conduction revealed a significant difference between traditional manufacturing and AM.

V. FUTURE WORK

Further investigation would focus on the four components making up the resistance measurements of the samples. The grain, interlayer, and electrode boundaries are areas available for further investigation. The additional components would allow for a more comprehensive comparison between a traditional sample and 3D-printed sample. Sample structural characterization and further densification measurements would prove helpful in determining how the printing and processing affect samples compared to traditional monolithic form of samples produced. The effects printing and debinding have on microstructure such as micro cracks would be a significant component in the comparison.

In addition, 3D-printing of multiple materials will be needed to assemble and manufacture device structures. This poses additional challenges of co-printing and co-sintering various materials of interest to devices.

VI. REFERENCES

1. Esposito, V.; Gadea, C.; Hjelm, J.; Marani, D.; Hu, Q.; Agersted, K.; Ramousse, S.; Jensen, S. H., Fabrication of thin yttria-stabilized-zirconia dense electrolyte layers by inkjet printing for high performing solid oxide fuel cells. *Journal of Power Sources* **2015**, 273, 89-95.
2. Huang, C.-C.; Su, P.-C.; Liao, Y.-C., Conductive lithium nickel oxide thin film patterns via inkjet printing technology. *Thin Solid Films* **2013**, 544, 348-351.
3. Kang, K.-Y.; Lee, Y.-G.; Shin, D. O.; Kim, J.-C.; Kim, K. M., Performance improvements of pouch-type flexible thin-film lithium-ion batteries by modifying sequential screen-printing process. *Electrochimica Acta* **2014**, 138, 294-301.
4. Kendall, K.; Kendall, M. High-temperature solid oxide fuel cells for the 21st century : *fundamentals, design and applications*. 2nd ed. ed.; Elsevier: London, **2016**.
5. *Solid oxide fuel cells : from materials to system modeling*. Royal Society of Chemistry: Cambridge, UK, **2013**.
6. Yashima, M.; Kakihana, M.; Yoshimura, M., Metastable-stable phase diagrams in the zirconia-containing systems utilized in solid-oxide fuel cell application. *Solid State Ionics* **1996**, 86-88, 1131-1149.
7. Laberty-Robert, C.; Ansart, F.; Deloget, C.; Gaudon, M.; Rousset, A., Dense yttria stabilized zirconia: sintering and microstructure. *Ceramics International* **2003**, 29 (2), 151-158.
8. Rajeswari, K.; Suresh, M. B.; Hareesh, U. S.; Rao, Y. S.; Das, D.; Johnson, R., Studies on ionic conductivity of stabilized zirconia ceramics (8YSZ) densified through conventional and non-conventional sintering methodologies. *Ceramics International* **2011**, 37 (8), 3557-3564.
9. Choudhary, A.; Sahu, B. S.; Mazumder, R.; Bhattacharyya, S.; Chaudhuri, P., Synthesis and sintering of Li₄SiO₄ powder from rice husk ash by solution combustion method and its comparison with solid state method. *Journal of Alloys and Compounds* **2014**, 590, 440-445.
10. Wu, X.; Wen, Z.; Xu, X.; Wang, X.; Lin, J., Synthesis and characterization of Li₄SiO₄ nano-powders by a water-based sol-gel process. *Journal of Nuclear Materials* **2009**, 392 (3), 471-475.
11. Izquierdo, M. T.; Turan, A.; García, S.; Maroto-Valer, M., Optimization of Li₄SiO₄ synthesis conditions by solid state method for maximum CO₂ capture at high temperature. *Journal of Materials Chemistry A* **2018**, 6, 3249–3257.
12. Adnan, S. B. R. S.; Mohamed, N. S., Citrate sol-gel synthesised Li₄SiO₄: conductivity and dielectric behaviour. *Materials Research Innovations* **2012**, 16 (4), 281-285.

13. Chang, C. C.; Wang, C. C.; Kumta, P. N., Chemical synthesis and characterization of lithium orthosilicate (Li_4SiO_4). *Materials & Design* **2001**, 22 (7), 617-623.
14. Masquelier, C.; Tabuchi, M.; Takeuchi, T.; Soizumi, W.; Kageyama, H.; Nakamura, O., Influence of the preparation process on the cation transport properties of $\text{Li}_4 + x\text{M}_x\text{Si}_1 - x\text{O}_4$ ($\text{M} = \text{B}, \text{Al}$) solid electrolytes. *Solid State Ionics* **1995**, 79, 98-105.
15. Liu, C.; Xu, F.; Cheng, X.; Tong, J.; Liu, Y.; Chen, Z.; Lao, C.; Ma, J., Comparative study on the electrochemical performance of LiFePO_4 cathodes fabricated by low temperature 3D printing, direct ink writing and conventional roller coating process. *Ceramics International* **2019**, 45 (11), 14188-14197.
16. Xu, H.; Cheng, W.; Jin, X.; Wang, G.; Lu, H.; Wang, H.; Chen, D.; Fan, B.; Hou, T.; Zhang, R., Effect of the Particle Size of Quartz Powder on the Synthesis and CO_2 Absorption Properties of Li_4SiO_4 at High Temperature. *Industrial & Engineering Chemistry Research* **2013**, 52 (5), 1886-1891.
17. Sivonxay, E.; Aykol, M.; Persson, K. A., The lithiation process and Li diffusion in amorphous SiO_2 and Si from first-principles. *Electrochimica Acta* **2020**, 331, 135344.
18. P v, S.; Nair, B.; Vijayan, V.; Ramakrishnan, S.; Peer, A.; Warrier, K.; Yamaguchi, T.; Hareesh, U. S., Germanium Incorporated Lithium Silicate as Highly Efficient Low Temperature Sorbents for CO_2 Capture. *Journal of Materials Chemistry A* **2018**, 6.
19. ASTM C20-00(2015), Standard Test Methods for Apparent Porosity, Water Absorption, Apparent Specific Gravity, and Bulk Density of Burned Refractory Brick and Shapes by Boiling Water, *ASTM International*, West Conshohocken, PA, **2015**, www.astm.org
20. Gates-Rector, S.; Blanton, T. The Powder Diffraction File: A Quality Materials Characterization Database. *Powder Diffr.* **2019**, 34 (4), 352–360. PDF4+ 2020.
21. Mücke, R.; Menzler, N. H.; Buchkremer, H. P.; Stöver, D., Cofiring of Thin Zirconia Films During SOFC Manufacturing. *Journal of the American Ceramic Society* **2009**, 92, S95-S102.
22. Lvovich, V. F., *Impedance spectroscopy : applications to electrochemical and dielectric phenomena*. Wiley: Hoboken, New Jersey, **2012**.
23. Brown, T. L.; H. Eugene LeMay, J.; Bursten, B. E.; Murphy, C. J.; Woodward, P. M.; Stoltzfus, M. W., Chemical Kinetics. In *Chemistry the central science*, 13 ed.; Jaworski, A., Ed. Pearson: Upper Saddle River, **2015**; pp 596-597.
24. Kwon, O. H.; Choi, G. M., Electrical conductivity of thick film YSZ. *Solid State Ionics* **2006**, 177 (35), 3057-3062.